A review of focused ion beam applications in optical fibers

Karen Sloyan,[1,2] **Henrik Melkonyan,**[3] **Harry Apostoleris,**[1,2] **Marcus S. Dahlem,**[4] **Matteo Chiesa,**[1,2,5] **and Amal Al Ghaferi**[1,2]

[1]Department of Mechanical and Materials Engineering, Khalifa University, SAN Campus, Abu Dhabi 127788, UAE
[2]Laboratory for Energy and Nano Science (LENS), Khalifa University, SAN Campus, Abu Dhabi 127788, UAE
[3]Department of Physics, Yerevan State University, Yerevan 0025, Armenia
[4]Interuniversity Microelectronics Center (IMEC), Leuven 3001, Belgium
[5]Department of Physics and Technology, UiT The Arctic University of Norway, Tromsø 9010, Norway

E-mail: karen.sloyan@ku.ac.ae

May 2021

Abstract. Focused ion beam (FIB) technology has become a promising technique in micro- and nano-prototyping due to several advantages over its counterparts such as direct (maskless) processing, sub-10nm feature size, and high reproducibility. Moreover, FIB machining can be effectively implemented on both conventional planar substrates and unconventional curved surfaces such as optical fibers, which are popular as an effective medium for telecommunications. Optical fibers have also been widely used as intrinsically light-coupled substrates to create a wide variety of compact fiber-optic devices by FIB milling diverse micro- and nanostructures onto the fiber surface (endfacet or outer cladding). In this paper, the broad applications of the FIB technology in optical fibers are reviewed. After an introduction to the technology, incorporating the FIB system and its basic operating modes, a brief overview of the lab-on-fiber (LOF) technology is presented. Furthermore, the typical and most recent applications of the FIB machining in optical fibers for various applications are summarized. Finally, the reviewed work is concluded by suggesting the possible future directions for improving the micro- and nanomachining capabilities of the FIB technology in optical fibers.

Keywords: focused ion beam (FIB) machining, optical fiber, nanostructures, lab-on-fiber (LOF) technology, nanofabrication

1. Introduction

Miniaturization of devices used in a variety of modern applications is accompanied by the development of advanced nanofabrication techniques, which can be classified into two categories: "bottom-up" and "top-down". The bottom-up approach is an additive manufacturing process, which uses atoms or molecules as the building blocks of nanostructures, while the top-down approach is a subtractive process, where the material is removed gradually to create features of a desired size and shape. The most widely used bottom-up methods include self-assembly (SA) [1, 2], photopolymerization [3, 4], chemical and physical vapor depositions (CVD and PVD) [5, 6], and atomic layer deposition (ALD) [7, 8], while the typical examples of top-down nanofabrication approaches are photolithography [9, 10], electron-beam lithography (EBL) [11, 12], focused ion beam (FIB) milling [13–15], nanoimprinting [16, 17], interference lithography [18, 19], and femtosecond laser ablation [20, 21].

Among the advanced top-down techniques, EBL and FIB machining are the two that ensure precise control over the entire patterning process, and enable direct (maskless) writing of sub-10nm features. EBL uses a focused beam of electrons to write 2D geometries in soft e-beam resists that are subsequently transferred onto the substrate by etching. This technique practically outperforms the conventional optical lithography (diffraction limited optical resolution), exploiting the ultra-short wavelength of the electrons. EBL nanopatterning has been effectively implemented for fabricating various nanostructures on traditional large and planar substrates [22–25]. The scenario substantially changes when dealing with unconventional substrates such as optical fibers. In particular, the use of EBL for patterning optical fibers becomes less effective since the traditional spin coating to produce a thin and uniform resist layer, and the etching for transferring the desired pattern onto the substrate become more challenging due to the curved surfaces, microscopic cross-section, large aspect ratio, and fragility of the fiber (especially glass optical fibers). This is where the FIB machining comes into play. Being a resistless fabrication technique, it ablates the material directly from the substrate, thus providing ease of patterning structures with an impressive spatial resolution on any irregular substrate. In contrast to EBL, heavy ions used in FIB machining also enable direct patterning on hard materials, including semiconductors, metals and ceramics. Moreover, the FIB milling technique is able to produce high-quality 2D and 3D micro- and nanostructures by precisely controlling their geometry [14, 15, 26–28]. The serial writing of this technique results in low throughput, which practically prevents its use for mass production (for this, photolithography is the most widely used technique). The FIB machining also suffers from some intrinsic drawbacks such as material redeposition and unintentional ion doping of the substrate. However, the FIB technology can still be effectively used for rapid prototyping high-resolution micro- and nano-structures on optical fiber substrates.

This review article mainly focuses on the FIB technology and its broad applications in optical fibers within last few decades. In Section 2, we briefly review the FIB system and the four basic principles of the FIB technology: milling, deposition, implantation, and imaging. The optical fiber properties and lab-on-fiber technology will then be discussed in Section 3. Section 4 overviews the most typical and interesting applications of the FIB machining in optical fibers for creating ultra-compact fiber-optic devices for various applications. In Section 5, the manuscript concludes with a discussion of possible future directions for enhancing the micro- and nanomachining capabilities of the FIB technology.

2. FIB technology

Developed since the early 1980s, the FIB technology was initially aimed at the semiconductor industry, where it has been extensively employed for failure analysis, circuit debugging, device modification, and lithographic mask repair [29–33]. However, since the 1990s the FIB instrument has also become a popular machining tool in other fields such as materials science and biochemistry. In particular, the FIB machining has been broadly used for preparing transmission electron microscopy (TEM) ultra-thin specimens [34–37], since it provides better control and reproducibility compared to the conventional electro-polishing and chemical polishing techniques [38–40], as well as allowing the preparation of specimens from a specific area in the substrate. Due to its versatility and nanoscale resolution, FIB machining has also been broadly used for rapid prototyping micro- and nanostructures for various applications in optics, optoelectronics, mechanics, atomic force microscopy etc. [32, 41–47]

2.1. FIB system

The basic parts of typical FIB systems are ion source, ion optics column, vacuum chamber and gas injection system (GIS). Conventional FIB instruments use high-brightness liquid-metal ion sources (LMIS) that can produce a beam spot on the order of 10 nm. The currently available ion sources include Au, Si, Ga, Al, As, Cu, Ge, Fe, In, Pt, and Pd. Among these, Ga is the most preferable ion source for FIB systems due to its low volatility, low melting point, heavy mass and electrical properties. It is worth noting that some other liquid metal alloy ion sources with lower melting

point such as PdAs, PdAsB, AuSi, AuSiB, NiB, and NiAs, have also been studied recently [48, 49]. On top of metal ion sources, plasma sources, which are still in a developing stage, have also been used in FIB instruments to boost the material sputtering rate with the respect to a conventional Ga^+ FIB using higher beam currents (µA) [50–52]. However, high currents result in large spot sizes, and thus lower spatial resolution. Therefore, plasma sources should be used in applications where the sputtering rate has more importance with respect to the milling resolution. Furthermore, gaseous ion sources such as He^+ gas field source have also been integrated into a FIB system for fabricating structures with higher spatial resolution over an LMIS FIB [53–55]. A He^+ ion source can provide ∼0.25 nm resolution and minimum feature size less than 5 nm [54, 55]. Nevertheless, in the case of a He^+ FIB, the bulk milling is quite slow due to the substantial low mass of helium ions. So, the trade-off between the milling rate and spatial resolution makes Ga^+ FIB systems most suitable for bulk milling. It is worth mentioning that He^+ FIB systems have great potential to replace Ga^+ FIB instruments in the near future, due to their smaller probe size and lower surface damage caused by the ion beam.

The application of a strong electric field accelerates the positively charged Ga^+ ions of a LMIS towards the target. They travel through the ion column composed of several beam-limiting apertures and condenser lenses. The latter are responsible for the beam formation, while the apertures define the beam current and spot size. The ion beam is ultimately focused on the specimen surface via objective lenses. When the beam hits the substrate surface, they lose energy to both the electrons and nuclei of the target atoms. Depending on the gained energy of the surface atoms, various interactions can occur between the incident ions and surface atoms, including milling, implantation, deposition, backscattering, amorphization, and nuclear reaction (Fig. 1) [54, 56].

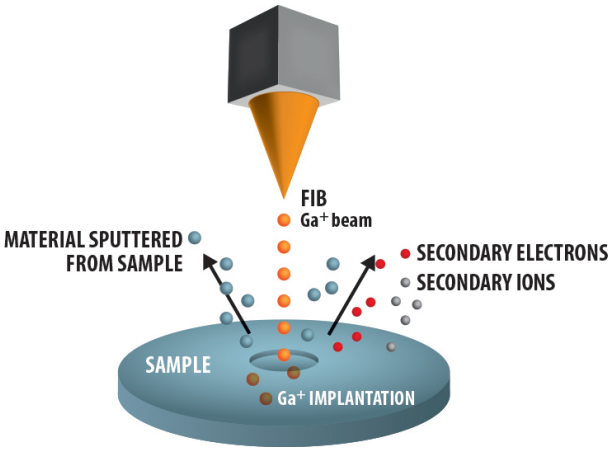

Figure 1: Schematic diagram of ion-target interactions.

2.2. FIB operating modes

In this section, the basic FIB operating modes such as milling, material deposition, ion implantation, and imaging resulting from ion-target elastic and inelastic collisions will be explained in more detail (Fig. 2).

2.2.1. FIB milling The ion-target elastic interactions result in FIB milling that incorporates physical sputtering, amorphization, and material redeposition (Fig. 2(a)). Physical sputtering occurs when the energy of surface atoms delivered by incident ions exceeds the surface binding energy. The sputtering yield, which is the number of atoms ejected from the sample surface per incident ion, mostly depends on factors such as masses of incident ions and specimen surface atoms, ion beam energy, and the incident angle of ions with respect to the target surface. In particular, the sputtering yield increases with the angle of incidence reaching its maximum near 80^o, and then abruptly decreases as the incident angle approaches 90^o [57, 58]. The sputtered atoms ejected from the sample surface into the gas phase are not totally removed from the vacuum chamber and are not at thermodynamic equilibrium, thus they tend to condense back into solid phase, and redeposit on the initially sputtered region. This practically lowers the effective sputtering rate, which can be boosted by introducing a gas inside the chamber during FIB milling. This process is called gas-assisted etching (GAE) [59, 60]. The redeposition effect can be reduced by optimizing various ion beam and processing parameters such as beam energy, ion current, dwell time, and incident angle. In the case of ion energies lower than the surface binding energy, amorphization may occur in the bombarded region of a crystalline substrate, when the incident ions are mainly buried in the substrate and may also displace the target atoms from their lattice positions.

2.2.2. Ion implantation On top of FIB milling, ion-matter interactions are also accompanied by ion implantation, which becomes dominant for high beam energies (Fig. 2(c)). In this case, the ions can easily penetrate deep into the substrate locally changing the material properties. The implantation depth strongly depends on the substrate material, ion beam energy, and probe current. Typical ion implantation depth can range from a few nanometers to a few tens of nanometers [61]. In particular, the depth of implanted ions at 30 keV for the glass optical fibers reviewed in this article, is ∼20 nm [62]. This implantation approach has been effectively used in microelectronics to introduce dopants into the semiconductors, as well

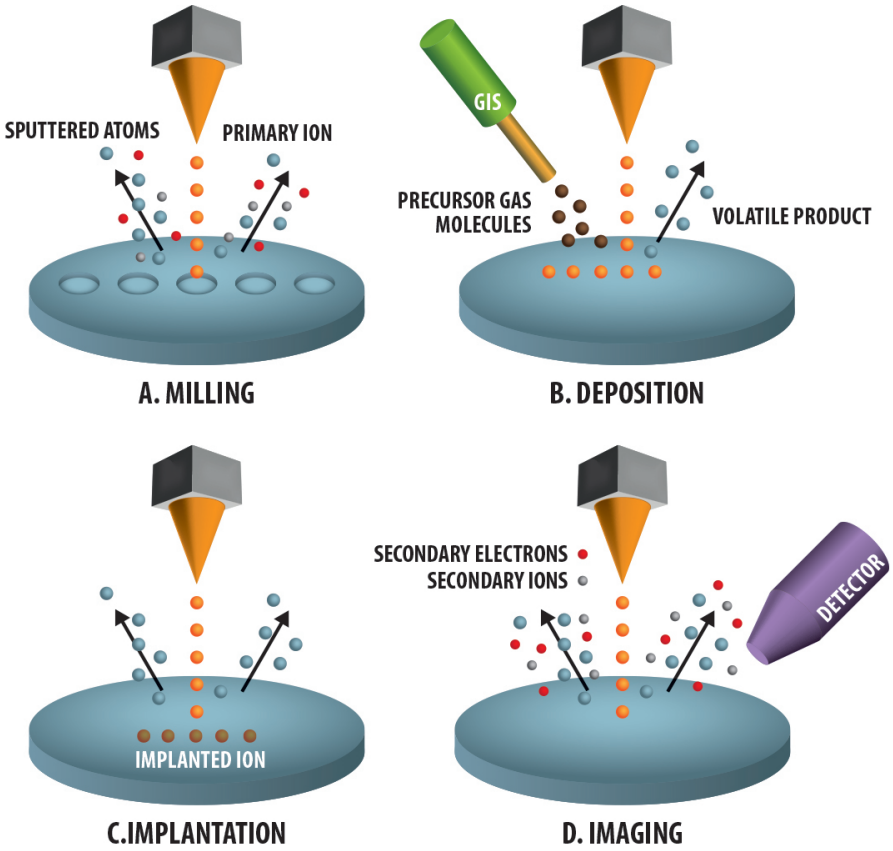

Figure 2: Basic functions of FIB technology.

as in the field of materials surface modification due to its control of distribution and concentration of dopants.

2.2.3. Material deposition FIB also allows deposition of various types of materials, including metals and insulators, in a very small region. The deposition process is performed by a gas injection system (GIS) (Fig. 2(b)). The gas is injected through a nozzle inserted very close to the sample surface in the vacuum chamber. After gas injection, the molecules adsorb on the surface of a target, and are decomposed into non-volatile products where the ion beam strikes, and volatile products far from the beam scanning area. The non-volatile species remain on the sample surface forming a deposition layer, while the volatile products are desorbed from the surface. FIB deposition can be controlled by few parameters, including scanning area, nozzle position, gas heating temperature, beam current, and dwell time. FIB metal (Au, Al, W, and Pt) deposition has been widely used in the semiconductor industry for making and repairing metal interconnects in lithographic masks [29, 30].

2.2.4. Imaging In contrast to elastic interactions, inelastic ion-target collisions transfer a part of the energy of the incident ions to the surface atoms. This leads to the emission of secondary electrons (SE) and secondary ions (SI) (Fig. 2(d)). The generated SEs can be collected for SEM imaging, while SIs for secondary ion mass spectroscopy (SIMS) to analyze the atomic composition of the target [63, 64]. It is worth mentioning that in comparison to SEs, due to their large size and positive charge, the SIs enable relatively lower resolution but higher contrast imaging. On the other hand, the high mass of ions inevitably damages the sample surface while imaging. For this reason, FIB/SEM dual-beam systems have been developed combining the FIB milling and non-destructive SEM imaging capabilities. The contemporary FIB/SEM dual-beam instrument is a vertical electron column with a tilted ion column, usually angled at 52^o (Fig. 3). This configuration practically allows real-time monitoring of the FIB machining process to assure the desired outcome. The dual-beam systems are usually used in the semiconductor industry for failure analysis of integrated circuits without damaging the nano-features [32].

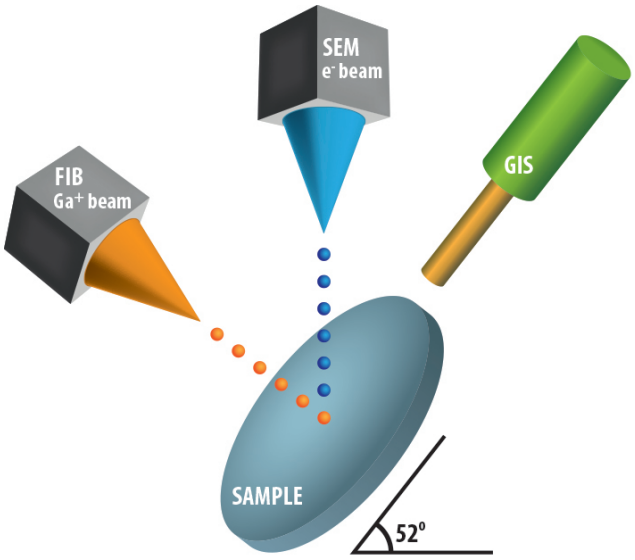

Figure 3: FIB/SEM dual-beam instrument.

3. LOF technology

An optical fiber is essentially a dielectric waveguiding structure most commonly made of high purity glass. It is composed of a cylindrical core, through which the light propagates, embedded in a slightly lower refractive index cladding to prevent the light from leaking (Fig. 4). Typical cladding diameter is 125 µm, while the core diameter mostly depends on the operational wavelength of the fiber, as well as the number of propagating modes the fiber can support (single- or multimode). The refractive index difference between the core and cladding confines the light signal in the core area of the fiber through total internal reflection (TIR), making it an optical waveguide. The purity of the glass material is the key to low-loss transmission of the signal. Even though glass is considered a fragile material, the outer jacket and strength member in addition to the polymer coating around the fiber successfully protects it from breaking and enables application in harsh environments (Fig. 4). The glass optical fiber is extensively used in telecommunication by enabling low-loss, high bandwidth and low cost transmission of information over long distance. In parallel to the development and advancements of fiber-optic communications, optical fibers have also managed to successfully replace bulk optical elements paving the way for the development of the lab-on-fiber (LOF) technology [65, 66].

In contrast to well-known lab-on-a-chip technology implemented on conventional planar substrates [67, 68], the LOF technology is a relatively new research area, aiming to integrate advanced functional materials and structures within unconventional fiber substrates using advanced nanofabrication techniques. This leads to a new light-coupled platform enabling the development of all-in-fiber multifunctional devices at the micro- and nanoscale. In general, the LOF platforms can be subdivided into three main categories (Fig. 5):

- **lab-on-tip**: the advanced materials and structures are integrated onto the fiber endfacet
- **lab-around-fiber**: the advanced materials and structural modifications are integrated onto the outer cylindrical curved surface of optical fibers
- **lab-in-fiber**: the functional materials are infiltrated within the holey structure of microstructured optical fibers (MOFs)

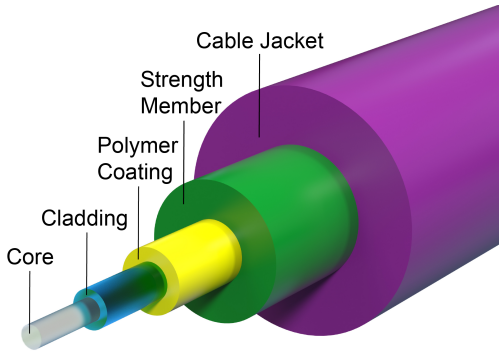

Figure 4: Schematic illustration of an optical fiber.

These non-conventional LOF platforms have been effectively used for fabricating a variety of compact fiber devices for diverse applications in lasing [69, 70], sensing [71, 72], and imaging [73]. In general, these devices have been fabricated using two different approaches. The first is a hybrid approach, comprised of the fabrication of functional materials and/or structures on planar substrates using well-developed nanofabrication techniques, and their consecutive integration onto an optical fiber via soft lithography, nanoskyving, and nanomanipulation techniques [74]. It is worth mentioning that the transferring step of the pre-fabricated structure or material, including detaching and bonding, is challenging and also has direct influence on the fabrication yield, and thus the performance of the created device. On the contrary, the second approach is based on the direct deposition and/or patterning of the advanced materials and/or structures on an optical fiber using "top-down" or "bottom-up" nanofabrication techniques such as CVD/PVD processing, sol–gel processing, self-assembly (SA), photopolymerization, chemical etching, EBL, interference lithography, femtosecond laser writing, nanoimprinting lithography, two-photon lithography, and FIB milling [74, 75].

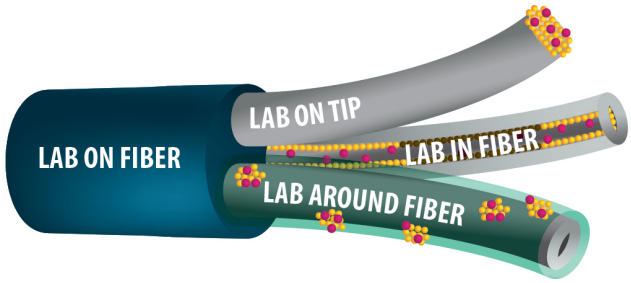

Figure 5: The lab-on-fiber paradigm.

In this paper, we review the applications of the FIB machining in the LOF technology. It is worth noting that the FIB technique was first applied on optical fibers in 1997 to create a near-field scanning optical microscopy (NSOM) fiber probe [76]. Thereafter, the FIB technology has been continuously developed and effectively used for fabricating diverse miniaturized lab-on-tip, lab-around-fiber, and lab-in-fber devices. This is evidenced by the bar chart illustrated in Fig. 6, showing the popularity and the trend of FIB applications in optical fibers within last few decades. In particular, FIB machining has been applied on the fiber tip to create NSOM probes [76–87], to pattern plasmonic nano-arrays [88–101] and beam shaping structures (lenses, zone and phase plates, holograms etc.) [102–121], as well as to fabricate microcantilevers [122–130]. It has also been effectively used to cleave and polish the fiber endfacet [131–137]. In addition, FIB machining has been employed for fabricating lab-around-fiber and lab-in-fiber devices such as micrograting [138–150], microcavities [151–160], as well as access holes and channels [161–169]. It is worth mentioning that the beam shaping structures fabricated on the fiber tip predominate in FIB applications in optical fibers (Fig. 7).

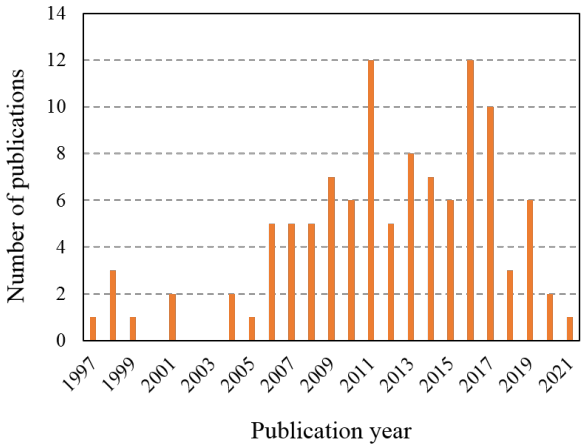

Figure 6: The trend of FIB applications in optical fibers within time.

It is also important to note that typical optical fibers being non-conductive materials are far from ideal substrates for FIB machining. Therefore, proper sample preparation is required to ensure high-quality fabrication. In particular, the fiber surface must be coated with a thin metal layer prior to FIB machining process in order to dissipate the charges built up on the surface during the process, since these accumulated charges can practically lead to deviation of the ions from the focused beam resulting in broadening of the spot, thus lowering the milling resolution.

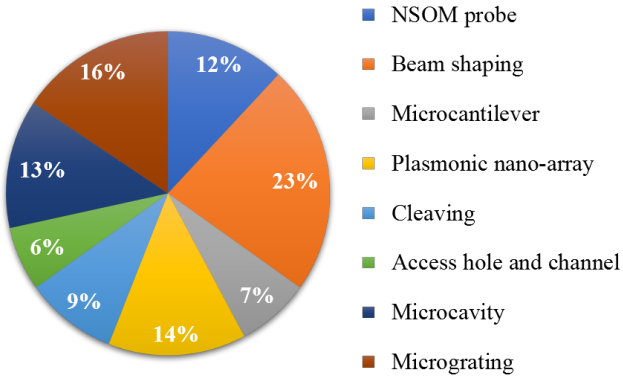

Figure 7: FIB applications in optical fibers.

4. FIB applications in optical fibers

In this section, we overview the most typical applications of the FIB technology in optical fibers for fabricating compact fiber-optic devices for a variety of applications. NSOM fiber probes, plasmonic nano-arrays, beam shaping structures, and microcantilevers are discussed first. Next, fiber cleaving by FIB is presented. The section will conclude with FIB-fabricated microgratings, microcavities, and access holes and channels.

4.1. NSOM fiber probes

The optical fiber probes used in near-field scanning optical microscopy (NSOM) can provide ultra-high resolution beyond the diffraction limit of conventional optical microscopes. The probe is generally a metal-coated (usually gold or aluminium) tapered optical fiber, where the tapering can be implemented either by heating-pulling or chemical etching methods [170–173]. In contrast to the widely used angled evaporation technique to create a subwavelength aperture at the apex of a tapered fiber [80], the FIB technology allows to mill an aperture of a desired shape and size directly on the very tip. The broadly used FIB drilling and FIB slicing techniques were first reported by Muranishi et al. in 1997 [76]. Later, these techniques were

extensively used to create apertures of different sizes and shapes (Fig. 8(a-b)) [77–81].

In parallel to the development and widespread use of the FIB machining, more complex near-field fiber probes were manufactured. In particular, Spajer et al. used FIB to fabricate a trihedral tip for NSOM by milling the three facets of the fiber tip (Fig. 8(c)) [82]. Afterwards, a more complex C-aperture was carved on the endfacet of a 45^o straw-shaped fiber probe for near-field applications [83]. Moreover, bowtie nano-aperture antennas were created on the tip of fiber probes by FIB direct milling for nanoimaging, nanolithography, and biosensing applications (Fig. 8(d)) [84, 85].

In 2016, a new "tip-on-aperture" (TOA) fiber probe was experimentally demonstrated by Kim and Chang, to enhance the optical resolution compared to conventional NSOM probes [86]. FIB milling was first used to create an aperture on the fiber tip, and then fabricate a triangular tip beside the aperture (Fig. 8(e)). To assess the resolution enhancement effect achieved by the fabricated TOA probe, a photoresist layer was raster scanned by the probe resulting in a pattern line of 50 nm (Fig. 8(f)). This was actually smaller than the size of the tip aperture (200 nm) due to the light confinement effects caused by the triangular shape tip.

Furthermore, a new in-situ FIB fabrication procedure was recently reported both to taper the fiber and drill an aperture on the very tip [87]. The fabrication of the fiber probe was carried out by few steps, where the ion beam current changed from one step to another, while the acceleration voltage was fixed at 30 kV during entire milling process. The tapering step was implemented using a beam current of 0.79 nA. Fig. 8(g) shows the FIB-fabricated probe after drilling an aperture. A detailed view of the probe is shown in Fig. 8(h), indicating an aperture of about 110 nm. Besides drilling an aperture of the desired diameter, this technique also enables the control of the cone apex angle for better optical throughput, as well as the length of the tapered region for improved mechanical robustness.

The dimensions and the FIB process parameters used for the fabrication of the aforementioned NSOM fiber probes are summarized in Table 1.

4.2. Plasmonic nano-arrays

Nano-arrays of subwavelength structures patterned in optically thick metallic films have become increasingly attractive due to the extraordinary light transmission through the nanostructures [174–176]. This is associated with the surface plasmons excited on the surface of arrays of nanostructures with a size smaller than the incident wavelength. Besides conventional planar substrates, these plasmonic nano-arrays have also been integrated onto the cleaved tips of optical fibers for various applications, including sensing [89, 91, 94] and surface-enhanced resonance Raman scattering (SERRS) [88, 95]. In contrast to planar substrates, this integration simplifies the optical alignment since the structures are defined directly on top of the fiber core. The easy identification of the core by wet etching enables the nanostructures to be precisely patterned on the core area improving the light transmission through the structures. The peaks of localized surface plasmon resonances (LSPR) can be tuned by varying the optical properties of the surrounding medium, as well as by controlling the size, the shape and the periodicity of the subwavelength nanostructures. The latter can be precisely controlled by using FIB. In this section, we present various plasmonic nano-arrays FIB-fabricated on the tips of optical fibers for diverse applications [88–101].

Nguyen et al. used FIB machining to fabricate an array of cross-shaped apertures on the tip of a single-mode fiber for refractive index sensing [94]. The fiber endfacet was first coated with a Au layer of 140 nm. 30 keV energy ions and 30 pA probe current were used to mill the nanoapertures. A high-magnification SEM image of an array of the cross-shaped apertures perforated in a gold film is shown in Fig. 9(a), where the arm-length, the arm-width and the periodicity of the cross-apertures were 300 nm, 20 nm, and 400 nm, respectively.

Andrade et al. experimentally demonstrated circular and bowtie-shaped nanohole arrays milled in gold films deposited on the tips of single-mode optical fibers for SERRS measurements [95]. Both arrays were patterned in a 100 nm-thick gold film using a beam current of 100 pA at 30 kV. The circular nanohole array was composed of 30×30 holes, while the array of bowties was a 40×40 matrix. The magnified views of both arrays are illustrated in Fig. 9(b-c). The diameter of circular nanoholes was 200 nm, while the array periodicity was 480 nm (Fig. 9(b)). For the bowtie structures, the long sides of the triangles, the distance between long sides of the triangles, and the separation between the triangles were measured as 200 nm, 420 nm, and 95 nm, respectively (Fig. 9(c)). The experimental results show that the SERRS enhancement efficiency of the bowtie-shaped nanostructures is higher than that of the patterned circular holes. Furthermore, a similar array of 80 nm-diameter circular holes patterned in a gold-coated fiber tip was also employed as a photoacoustic ultrasound generator for ultrasonic applications [96].

FIB machining was also used for the integration of metasurfaces on the fiber tips. In particular, Xomalis et al. reported an all-fiber switching metadevice [98]. The plasmonic metamaterial was composed of

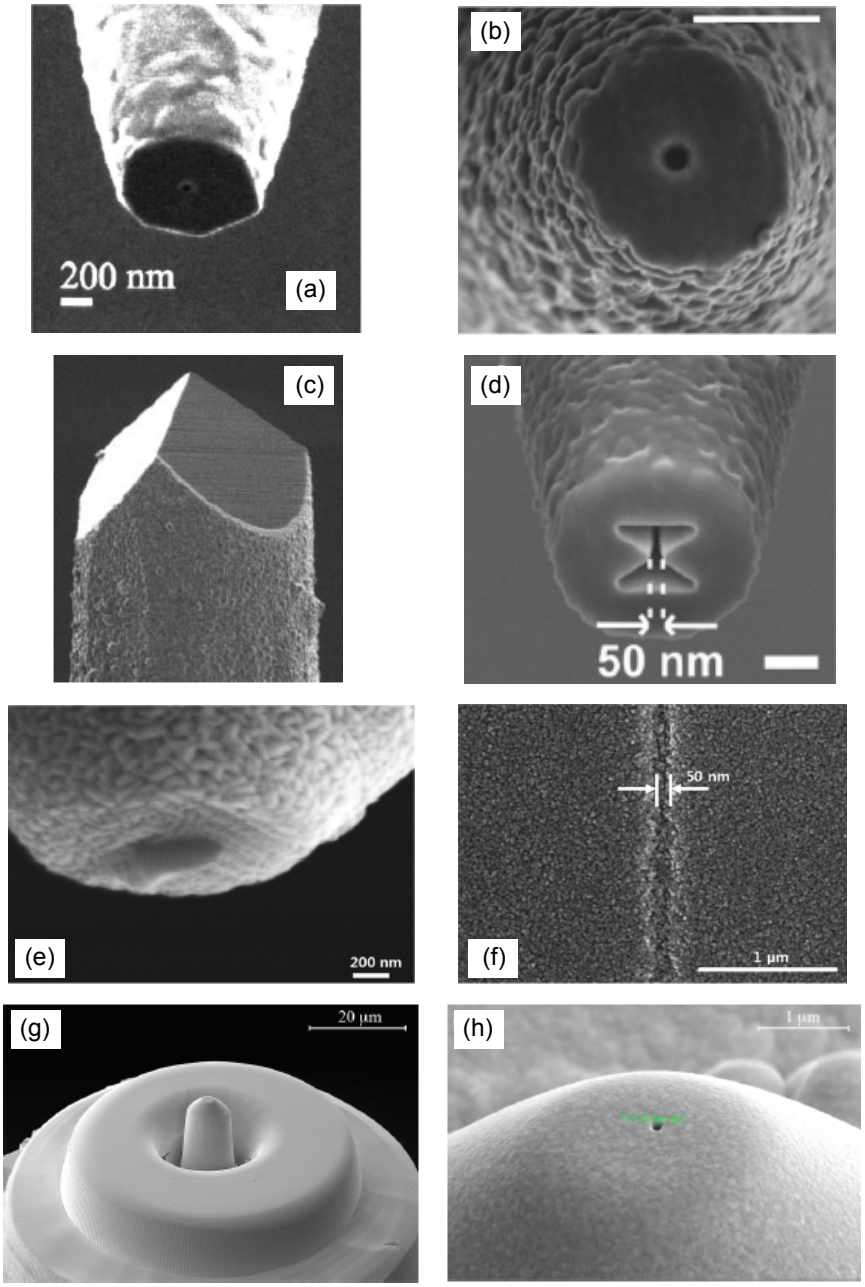

Figure 8: NSOM fiber probes fabricated using FIB machining. (a) FIB image of a fiber probe with an aperture diameter of 35 nm [78]; (b) SEM image of a probe with a 110 nm aperture on the very tip (the scale bar is 500 nm) [81]; (c) FIB image of a trihedral tip [82]; (d) SEM image of a bowtie nanoaperture milled in the fiber endfacet (the scale bar is 200 nm) [85]; SEM images of (e) a TOA probe with a triangular pyramid tip and (f) the line pattern fabricated using the probe [86]; SEM images of (g) a tapered fiber probe and (h) an aperture of 110 nm drilled on the probe tip [87].

an array of asymmetrically split ring apertures milled in a 70 nm-thick gold film. The nanostructures were patterned by FIB milling on a 25 µm x 25 µm area covering the core of a polarization-maintaining single-mode fiber (Fig. 9(d)). Furthermore, a phase-gradient plasmonic metasurface was patterned on the endfacet of a single-mode optical fiber that allows steering of the light beam impinging from the fiber core in desired directions [97]. A 50 pA beam current at 30 kV was used to mill the desired pattern of rectangular holes in a 50 nm gold layer covering the fiber core region (Fig. 9(e)). FIB was also used to fabricate a metalens on the gold-coated endfacet of a photonic crystal fiber (PCF), which allows to focus the circularly polarized incident beam [101]. An acceleration voltage of 30 kV and a beam current of 1.5 pA were used for fabricating

Table 1: **Summary of FIB-fabricated NSOM fiber probes (d - aperture diameter, l - length)**

Aperture	Size	FIB process parameters	Applications	Ref.
Circular	-	Ga, 30 kV, 20 pA	NSOM	76
Elliptical	100 nm x 300 nm	Ga, 30 kV, 12 - 70 pA, 10 - 20 sec	NSOM	79
Circular	d_1 = 100 nm, d_2 = 300 nm	Ga, 30 kV	NSOM	77
Circular	d_1 = 200 nm, d_2 = 35 nm	Ga, 30 kV, 11 pA	NSOM	78
Trihedral tip	-	-	NSOM	82
C-shape	300 nm x 200 nm	-	NSOM	83
Bowtie	-	-	NSOM	84
Circular	d = 200 nm	Ga, 40 kV, 10 pA	Sensing	80
Circular	d_1 = 110 nm, d_2 = 45 nm	-	NSOM	81
Bowtie	l = 300 nm, gap between arms = 50 nm	-	Nanoimaging	85
Triangular pyramid tip	curvature at the tip end = 50 nm	Ga	NSOM	86
Circular	d_1 = 250 nm, d_2 = 110 nm	Ga, 30 kV, 0.79 nA	NSOM	87

the metalens (Fig. 9(f)).

Kim et al. proposed a fiber-optic LSPR sensor by patterning a nanodisk array in a gold film deposited on the tip of a multimode optical fiber [99]. In order to avoid the larger area FIB-fabrication on the 50 µm diameter fiber core, and hence to reduce fabrication time, a lift-off technique was used to remove the gold layer left on the core using an Al sacrificial layer. A 100 nm-thick Al film was first deposited on the fiber tip. A 20 µm x 20 µm region of Al layer at the center of the tip was subsequently milled away by FIB. After plasma cleaning and deposition of an adhesion layer, the fiber tip was coated with a 30 nm of Au film. Next, a 66 × 66 array of nanodisks with a 70 nm diameter and a 200 nm gap was patterned by FIB machining followed by the Al layer removing through the lift-off method (Fig. 9(g)). FIB machining was also applied on the fiber tips for patterning arrays of nanorods, nanopillars, and nanogratings [88–93].

The dimensions and the FIB process parameters used for the fabrication of the aforementioned plasmonic nano-arrays are summarized in Table 2.

4.3. Beam shaping structures

Beam shaping structures fabricated on the fiber tip through FIB machining dominate FIB applications in optical fibers (Fig. 7) [102–121]. The role of these structures are to shape the light beam exiting the optical fiber. They have been mostly targeted for two main applications: optical tweezing [103, 104, 106–109, 111, 112, 116, 117, 121] and fiber-to-chip light coupling [102, 113–115, 120].

4.3.1. Beam shaping structures for optical tweezing

Optical tweezers (OTs) are powerful tools widely used in physics, biology, chemistry, and force spectroscopy [177]. Focusing the laser beam, OTs can manipulate and trap micrometer-sized particles by exploiting the forces exerted by the focused beam. Optical manipulation was first proposed by Ashkin et al. in 1970 [178]. Within last few decades, the OTs have been successfully integrated on the tip of optical fibers (OFT) creating miniaturized and compact fiber devices for a variety of applications [103, 104, 106–109, 111, 112, 116, 117, 121].

The rapid divergence of the Gaussian beam used in conventional OTs limits the active trapping region, and thus lowers the efficiency of the tool. Cabrini et al. fabricated a microaxicon on the tip of a Ge-doped SiO_2 fiber by using FIB machining to convert the guided Gaussian mode of the fiber core into a Bessel-like beam with an extended depth of focus, resulting in an enlarged trapping region [103]. A 30 kV accelerating voltage and a 0.5 nA beam current were used to create an axicon structure with a base diameter of 10 µm and a height of 5 µm at the center of the fiber core (Fig. 10(a)). The total milling took 3 hours.

A Bessel-like profile for optical micro-manipulation was also achieved by a plasmonic lens composed of a subwavelength slit-metallic groove structure, FIB-milled in the gold-coated tip of a coreless silica fiber [106]. A similar plasmonic structure consisting of double parallel slits combined with graded groove arrays was also fabricated on the metal-coated fiber tip for generating Airy beams for potential applications in optical trapping (Fig. 10(b)) [108].

Plasmonic structures defined on the fiber tip were also used for 3D trapping. In particular, Berthelot et al. demonstrated 3D optical manipulation of sub-100 nm dielectric objects with a near-field nanotweezer [109]. The latter was fabricated by milling a bowtie nanoaperture in the tapered metal-coated fiber tip (Fig. 10(c)). In addition, 3D trapping of subwavelength particles was experimentally demonstrated by using a surface plasmon (SP) fiber lens [107]. The SP lens was composed of concentric subwavelength slits FIB-milled in the gold-coated fiber tip (Fig. 10(d)). The variation of the slit width here ensures the phase difference of the SP modes for far-field superfocusing, which allows trapping about 6 wavelengths away in contrast to near-field optical tweezers.

Later, various beam shaping structures, including

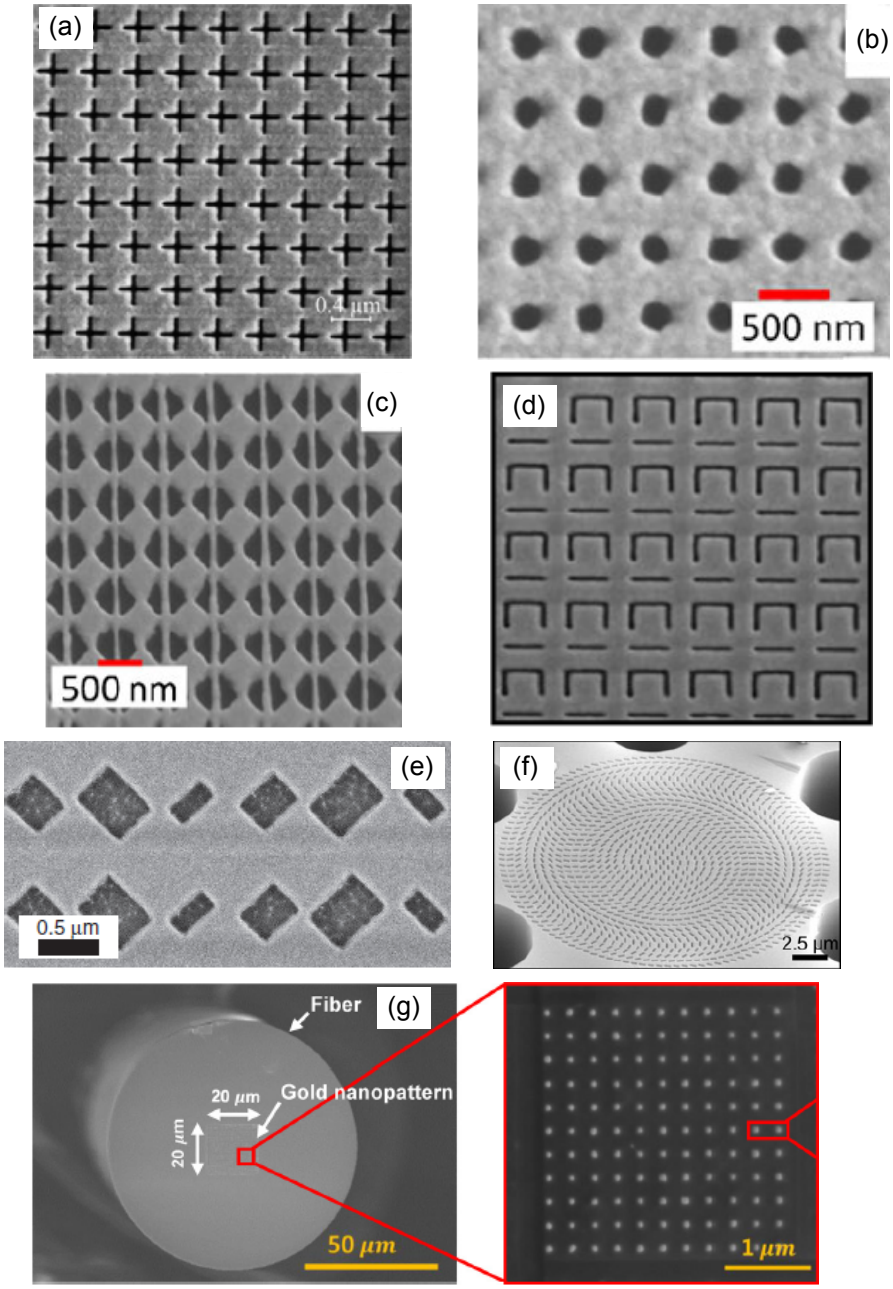

Figure 9: SEM images of plasmonic nano-arrays fabricated on the fiber tips by FIB machining. (a) an array of cross-apertures [94]; (b) circular and (c) bowtie-shaped hole arrays [95]; (d) an array of asymmetrically split ring apertures (the scale bar is 1 µm) [98]; (e) a phase-gradient metasurface composed of an array of rectangular holes [97]; (f) a photonic crystal fiber metalens [101]; (g) a gold nanodisk array [99].

Fresnel zone/phase plates (Fig. 10(e-f)) [116, 117] and spiral zone/phase plates (Fig. 10(g-h)) [111, 112, 121] were patterned on the fiber tip by FIB as promising candidates for particle manipulation and optical trapping.

The dimensions and the FIB process parameters used for the fabrication of fiber-top beam shaping structures for optical tweezing are summarized in Table 3.

4.3.2. Beam shaping structures for fiber-to-chip light coupling Optical fibers have also been extensively used to couple laser beams into silicon photonic chips due to the difficulties in creating efficient light source on silicon (indirect bandgap). The mode size mismatch between a silicon waveguide and a single-mode optical fiber results in coupling losses that need to be addressed for efficient fiber-to-chip light coupling. One of the promising approaches to lowering the

Table 2: **Summary of plasmonic nano-arrays FIB-patterned in the metal-coated endfacet of optical fibers (s - array area, d - hole diameter, l - feature length, w - feature width, t - metal thickness, Λ_x - horizontal periodicity, Λ_y - vertical periodicity)**

Feature	Dimensions	FIB process parameters	Applications	Ref.
Rod	s = 62.5 µm x 62.5 µm, t = 35 nm, w = 80 nm, l = 165 nm, Λ_x = 160 nm, Λ_y = 195 nm	Ga	Sensing, SERS	88
Circular hole	s = 24 x 24, t = 180 nm, $\Lambda_x = \Lambda_y$ = 600 nm, d = 200 nm	Ga, 40 kV, 10 pA	Sensing	89
1. Circular pillar 2. Square pillar	1. s = 4 x 4, t = 200 nm 2. s = 8 x 8, t = 50 nm	Ga, 40 kV	Sensing	90
Grating	s = 12 µm x 12 µm, t = 80 nm, Λ_x = 200 nm, w = 100 nm	Ga, 30 kV	Sensing	93
1. Circular hole 2. Bowtie hole	1. s= 30 x 30, d = 200 nm 2. s= 40 x 40, t = 100 nm	Ga, 30 kV, 100 pA	SERRS	95
Cross aperture	s = 30 x 30, w = 20 nm, l = 300 nm, t = 140 nm, $\Lambda_x = \Lambda_y$ = 400 nm	Ga, 30 kV, 30 pA	Sensing	94
Circular hole	d = 80 nm, t = 60 nm, $\Lambda_x = \Lambda_y$ = 200 nm	Ga, 30 kV	Ultrasonic	96
Rect. hole	t = 50 nm	30 kV, 50 pA	Imaging, Sensing	97
Disk	s = 66 x 66, t = 30 nm, d = 70 nm, $\Lambda_x = \Lambda_y$ = 270 nm	Ga, 30 pA	Sensing	99
Asymmet. split ring aperture	s = 25 µm x 25 µm, t = 70 nm	-	Switching	98
Rect. hole	t = 40 nm	Ga, 30 kV, 10 pA	Imaging, Sensing	101
Crystal cavity	t = 60 nm	-	Sensing	100

Table 3: **Summary of beam shaping structures FIB-fabricated on the endfacet of optical fibers for optical tweezing (s - area, d - diameter, w - width, l - length, h - height, t - metal thickness, R - ring radius, N_s - number of slits, N_g - number of grooves, w_g - groove width, Λ - groove period, h_g - groove depth)**

Structure	Dimensions	FIB process parameters	Applications	Ref.
Axicon	d = 10 µm, h = 10 µm	Ga, 30 kV, 0.5 nA, 3 hours	Optical tweezing	103
Trapezium hole	s = 150 µm^2, h = 10 µm	20 nA	Optical tweezing	104
Slit-metallic groove	w = w_g = 50 nm, l = 10 µm, N_s = 1, N_g = 150, h_g = 80 nm, Λ = 800 nm, t = 240 nm	-	Optical tweezing	106
Concentric ring slit	t = 100 nm	-	Optical tweezing	107
Slits-metallic grooves	w_s = 130 nm, w_g = 260 nm, t = 200 nm, h_g = ∼70 nm, N = 70	-	Optical trapping	108
Bowtie	t = 100 nm, gap between arms = 85nm	-	3D trapping	109
Spiral phase plate	d = 10 µm, h = 1.26 µm	Ga, 30 kV, 0.3 nA	Optical trapping	111
Spiral phase plate	d = 8 µm, h = 1.6 µm	0.1 nA, 29 min	Optical trapping	112
1. FZP 2. FPP	1. t = 20 nm	1. Ga, 0.3 nA, 41 sec 2. Ga, 0.1 nA, 15 min	Optical trapping	116
Metallic FZP	R_{in1} = 3.33 µm, R_{out1} = 4.72 µm R_{in2} = 5.8 µm, R_{out2} = 6.72 µm R_{in3} = 7.54 µm, R_{out3} = 8.29 µm R_{in4} = 8.98 µm, R_{out4} = 9.64 µm R_{in5} = 10.25 µm, R_{out5} = 10.84 µm R_{in6} = 11.41 µm, R_{out6} = 11.95 µm t = 100 nm	-	Optical trapping, Sensing	117
Spiral	d = 62.5 µm, h = 1.577 µm	30 kV, 7 nA	Particle manipulation	121

fiber-to-waveguide coupling losses is the use of beam shaping structures to focus the mode-field diameter exiting the optical fiber into a smaller spot. As an alternative to commercial tapered lensed fibers [179], various fiber-top lenses fabricated by FIB machining were presented for efficient fiber-to-chip light coupling [102, 113–115, 120].

In particular, a diffractive spherical lens composed of 10 circular crowns with different diameter and thickness was fabricated on the tip of a single-mode optical fiber by FIB technique for fiber-to-$LiNbO_3$ waveguide light coupling (Fig. 11(a)) [102]. The lens with a diameter of 15 µm allowed the fiber mode size to be reduced from 10.5 µm to around 5.2 µm, which enabled significant coupling improvement to be achieved over direct coupling.

Another diffractive optical element in the form of a phase photon sieve was reported by Janeiro et al. for light coupling to silicon photonics waveguides (Fig. 11(b)) [113]. An acceleration voltage of 30 kV

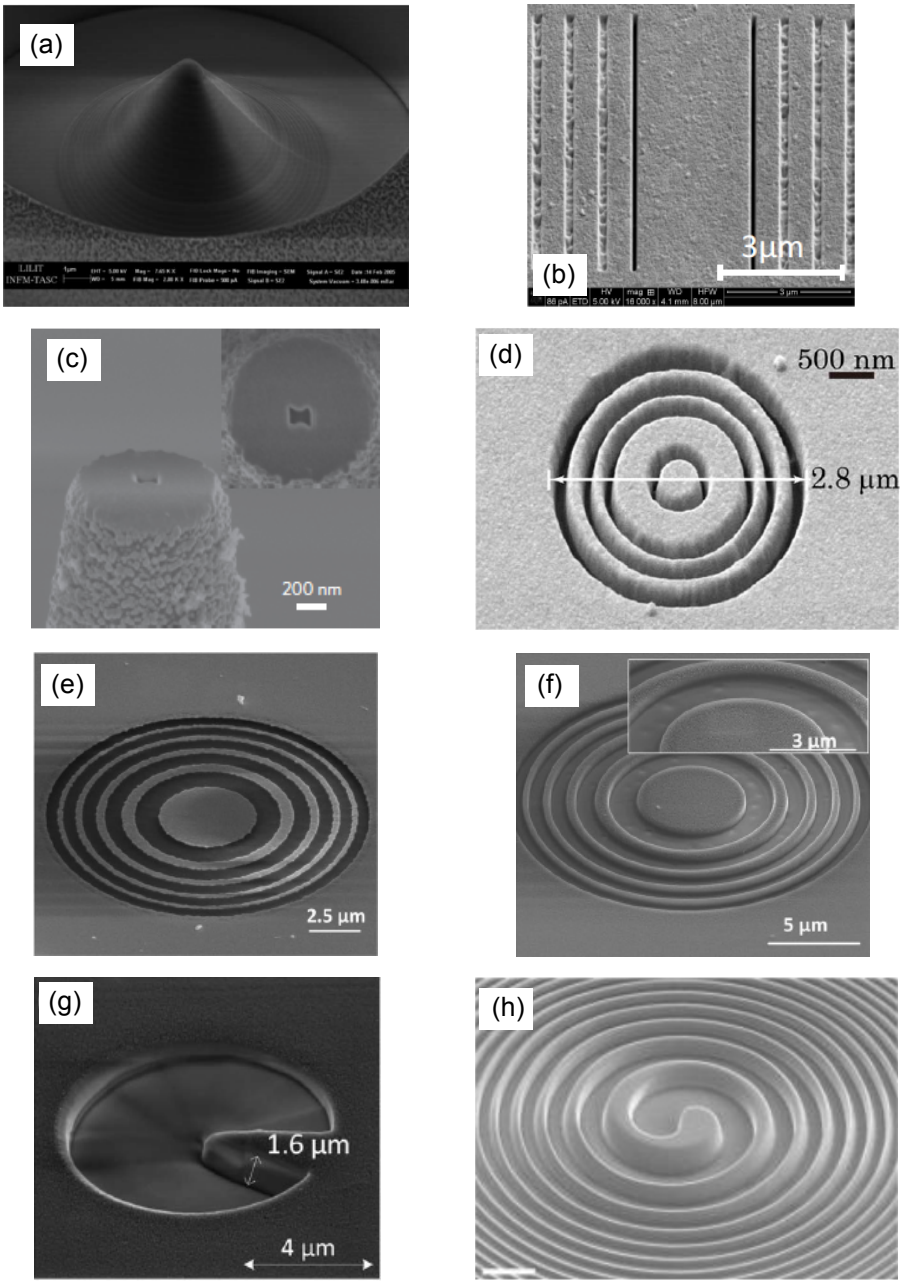

Figure 10: SEM images of beam shaping structures FIB-milled in the fiber tips for optical manipulation and trapping. (a) a 5 µm-high axicon [103]; (b) double parallel slits and graded grooves arrays [108]; (c) an 85 nm-gap bowtie aperture [109]; (d) a surface plasmon lens composed of four concentric rings [107]; Fresnel (e) zone and (f) phase plates [116]; spiral (g) phase and (h) zone plates (the scale bar is 10 µm) [112, 121].

and a beam current of 0.5 nA were used for fabricating the photon sieve. The total milling took 20 min. The photon sieve defined on the fiber tip enabled higher alignment tolerance and improved coupling efficiency.

Fiber-to-chip light coupling was also demonstrated by using a gradient-index fiber lens (Fig. 11(c)) [114]. The first two rings of the lens were milled using a beam current of 10 pA at 30 kV, while 49 pA current was used for the remaining rings. It is worth noting that the different aspect ratios of the concentric rings resulted in different depth and shape profiles of the milled trenches (Fig. 11(d)). The fabricated lens allowed to reduce the mode-field diameter exiting the fiber into smaller spot sizes, which in turn ensured a coupling efficiency comparable to a commercial lensed fiber.

Furthermore, a similar axicon structure demonstrated for optical trapping [103] was also reported for

fiber-to-waveguide edge coupling [115]. 30 kV acceleration voltage and 0.5 nA beam current were used for fabricating a 5 µm-high fiber axicon lens. An SEM image of the fabricated axicon lens is shown in Fig. 11(e). This lens offers relatively large longitudinal alignment tolerance due to the extended depth of focus of the Bessel-type beam. Later, a FIB-patterned parabolic lens embedded below the endfacet of a single-mode fiber was experimentally demonstrated [120]. Using a 0.23 nA probe current, the lens with a diameter of 15 µm and a height of 5 µm was milled 6.5 µm below the fiber tip, where the depth corresponded to the focal length of the lens (Fig. 11(f)). This simplifies the longitudinal and angular alignments for fiber-to-waveguide light coupling.

The dimensions and the FIB process parameters used for the fabrication of fiber-top beam shaping structures for fiber-to-chip light coupling are summarized in Table 4.

4.4. Microcantilevers

Free hanging cantilevers have found broad applications in a variety of research fields such as position sensing, topography measurements, and biochemical manipulations [122, 180, 181]. FIB machining has been effectively employed to integrate the cantilevers onto the tip of an optical fiber for creating miniaturized fiber sensors [122–130]. The fiber-top cantilever is usually positioned to cover the core area of an optical fiber, and therefore the laser light coupled to the core is partially reflected back into the fiber by the cantilever. The reflected light can be further enhanced by coating the top of the cantilever with a metal. It is also important to note that the monolithic fiber-top cantilevers overcome the alignment difficulties making them attractive for diverse applications.

Iannuzzi et al. used FIB to fabricate a fiber-top cantilever composed of a 3.7 µm-thick, 14 µm-wide and 112 µm-long rectangular beam free-hanging at one end of the fiber endfacet (Fig. 12(a)) [122]. Later, they added a pyramidal tip on the top of its free hanging end making an AFM probe (Fig. 12(b)) [123]. An ion beam current of 21 nA at 30 kV was used to mill the cantilever followed by the fine milling of the pyramidal tip using a lower 100 pA beam current. The total milling took less than 4 hours. The fabricated fiber-top AFM in contact mode shows performance comparable to commercially available AFM systems. The same group also reported a micro-cantilever fixed at both ends at the fiber tip creating a fiber-top refractometer (Fig. 12(c)) [126].

Furthermore, Li et al. fabricated various microcantilevers onto the top of an optical fiber as temperature [128] and pH [129] sensors. In this case, a picosecond (ps) pulsed laser was first used to remove large volumes of material, and thus to reduce the total FIB fabrication time. The FIB machining was subsequently involved to thin the cantilever, and thus improve the sensitivity (Fig. 12(d)). The FIB milling also allows much lower surface roughness to be achieved. In addition to fiber-top cantilevers, FIB machining was also used for fabricating a cantilever onto the side of an optical fiber for acceleration measurement [130].

FIB technology was also employed to fabricate microcantilevers sensitive to temperature and vibration [127]. The specially designed and doped optical fibers were first etched by hydrofluoric (HF) acid resulting in microwires with a diameter of 15 µm. Two different cavity structures were subsequently milled in the microwires: a 167 µm-long indentation as a temperature sensor, and a totally cleaved (suspended on one end) microwire cantilever with a length of ∼1025 µm for temperature and vibration sensing (Fig. 12(e)).

The dimensions and the FIB process parameters used for the fabrication of fiber microcantilevers are summarized in Table 5.

4.5. Cleaving

Maintaining a smooth and clean tip surface of an optical fiber is essential for high quality patterning, as well as low-loss butt-coupling between two fibers. Most of the commercial fiber cleaving tools are mechanical using a sharp blade made of various materials, including diamond and sapphire. While they are considered for rapid cleaving, the mechanical process usually results in some micro-cracking on the fiber endfacet and rough edges on the fiber cladding [132, 133]. Exceptionally smooth and clean fiber cross-sections can be achieved by FIB machining due to its high resolution and precise submicron control.

FIB milling was first employed for cleaving tapered fiber tips in 1999 [131]. By cleaving at different points along the fiber axis, the mode evolution in single-mode fibers was studied. Afterwards, Gibson et al. used a FIB/SEM dual-beam system to cleave and characterize the hole-array structure in tapered photonic crystal fibers (PCF) (Fig. 13(a)) [132]. The same technique was also used by Li et al. to cleave a PCF without damaging the microstructured air-hole structure in silica [133]. The entire milling process was performed in few steps: first, the incident angle of Ga ions was adjusted with respect to the fiber axis; second, rough milling was performed using a beam current of 6.4 nA (Fig. 13(b)). A lower current of 0.25 nA was subsequently used to polish the cleaved facet (Fig. 13(c)). The total milling took around 8 hours. The resulting smooth endfacet allowed a low-loss splice between the PCF and a conventional step-index optical fiber for further measurements of low gas

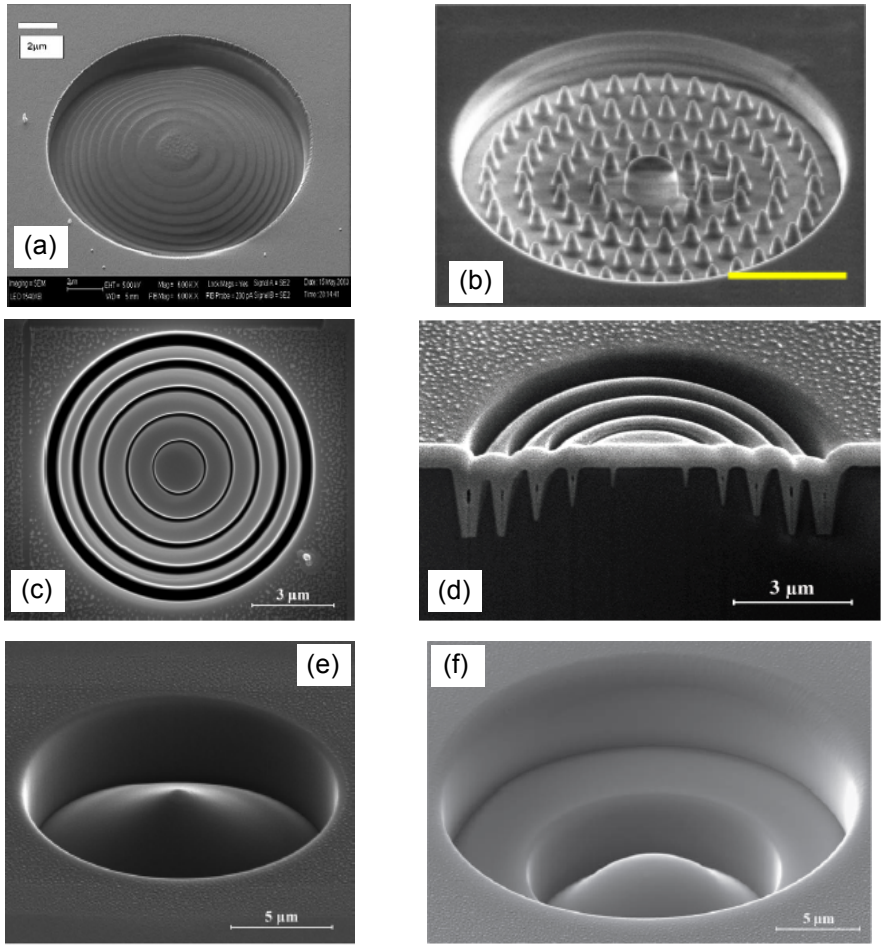

Figure 11: SEM images of beam shaping structures FIB-milled in the fiber tips for fiber-to-chip light coupling. (a) a diffractive spherical lens with a diameter of 15 µm [102]; (b) a phase photon sieve (the scale bar is 5 µm) [113]; a gradient-index lens composed of five concentric rings: (c) top and (d) cross-section view of the fabricated lens [114]; (e) a 5 µm-high axicon lens [115]; (f) a 5 µm-high embedded parabolic lens [120].

Table 4: **Summary of beam shaping structures FIB-fabricated on the endfacet of optical fibers for fiber-to-chip light coupling (d - diameter, h - height, Λ - ring period)**

Structure	Dimensions	FIB process parameters	Applications	Ref.
Spherical lens	d = 16 µm, h = 1 µm	Ga, 30 kV	Light coupling	102
Phase photon sieve	d = 16.5 µm, h = 1.73 µm	Ga, 30 kV, 0.5 nA, 20 min	Light coupling	113
Concentric rings	d = 10 µm, h = 1.25 µm, Λ = 1 µm	Ga, 30 kV, 49 pA	Light coupling	114
Axicon	d = 15 µm, h = 5 µm	Ga, 30 kV, 0.5 nA	Light coupling	115
Parabolic lens	d = 15 µm, h = 5 µm	Ga, 30 kV, 0.23 nA, 2 hours	Light coupling	120

concentrations. The same research group later used the FIB technology for PCF angle cleaving [134]. The fiber tip was cut at 45^o to minimize the interference of reflections (Fig. 13(d)). Moreover, Wang et al. demonstrated transmission-enhanced glass fiber tips cleaved at angles of 30^o, 40^o and 45^o [135].

In contrast to widely used glass optical fibers, the cleaving of polymer optical fibers via conventional mechanical tools is more challenging since the fibers can easily get damaged and deformed. In this case, the high-precision FIB milling technique can be effectively employed for making smooth cuts of polymer fibers. Comparing various cleaving techniques for single-mode polymer optical fibers, Abdi et al. showed the effectiveness of FIB machining in spite of the time required for fiber cleaving [136]. The FIB cleaving was also experimentally demonstrated for polymer porous fibers [137]. An acceleration energy of 30 keV and a probe current of 21 nA were used to cleave spider-web (Fig. 13(e)) and rectangular (Fig. 13(f)) porous fibers resulting in smooth cross-sections of the fiber endfacet. The cleaving process for a porous fiber with a diameter

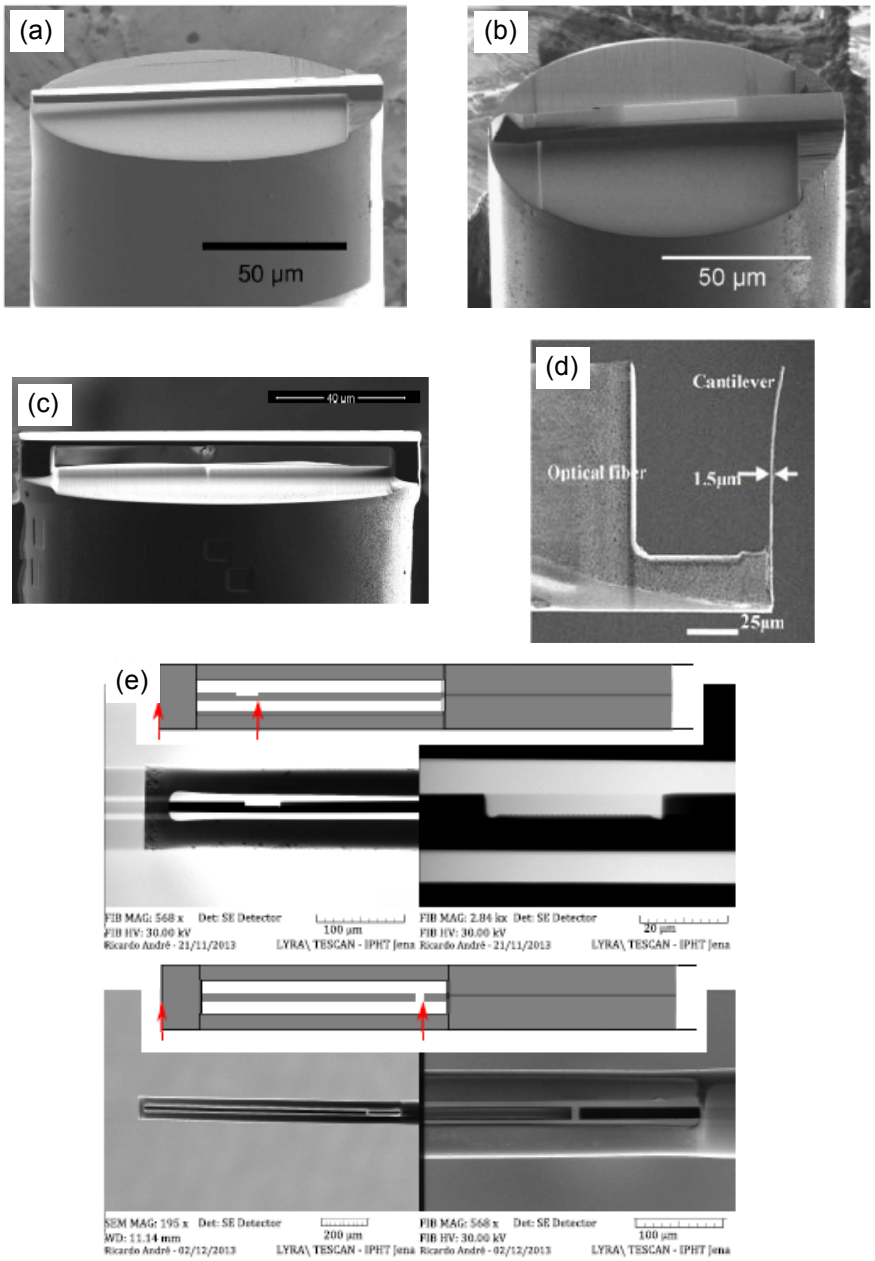

Figure 12: FIB-fabricated fiber microcantilevers. (a) SEM image of a 12 µm-long, 14 µm-wide, and 3.7 µm-thick fiber-top cantilever [122]; (b) SEM image of a fiber-top AFM probe [123]; (c) FIB image of a 2.5 µm-thick cantilever fixed at both ends at the fiber tip [126]; (d) SEM image of a microcantilever [129]; (e) SEM images of a 167 µm-long indented cavity (top) and a suspended microwire cantilever with a length of 1025 µm (bottom) [127].

of 400 µm took around 17.5 hours.

The fiber diameter and the FIB process parameters used for fiber cleaving are summarized in Table 6.

4.6. Micrograting

A fiber micrograting is a diffraction grating with a periodic change of refractive index in the core and/or cladding of an optical fiber. Fiber gratings have been extensively used in optical communication [182–184], as well as in sensing applications for measuring various parameters such as temperature, strain and refractive index [185–190]. Based on the period of the refractive index modulation, fiber gratings can be classified as short period with a sub-micrometer modulation period or long period (LPFG) having a period of a few hundreds of micrometers (Fig. 14). The most common example of a short period fiber grating is the fiber

Table 5: **Summary of FIB-fabricated fiber microcantilevers (w - cantilever width, l - cantilever length, t - cantilever thickness, g - fiber to cantilever gap)**

Structure	Dimensions	FIB process parameters	Applications	Ref.
Fiber-top cantilever	w = 14 µm, l = 112 µm, t = 3.7 µm	-	Position sensing	122
Fiber-top cantilever	-	-	Contact mode AFM	123
Fiber-top cantilever	-	Ga, 30 kV, 21 nA, 4 hours	Position sensing	124
Fiber-top cantilever	t = 2.5 µm, g = 8 µm	-	Refractive index sensing	126
Fiber-top cantilever	l_1 = 167 µm l_2 = 1025 µm	Ga, 1 nA	Temperature and vibration sensing	127
Fiber-top cantilever	w = 2 µm, l = 110 µm	Ga, 30 kV, 15 nA, ∼20 min	Temperature sensing	128
Fiber-top cantilever	w = 18 µm, l = 100 µm, t = 1.5 µm	30 kV, 30 nA/7 nA, ∼20 min	pH sensing	129
Fiber-side cantilever	w = 35 µm, l = 1 mm, t = 6 µm	-	Acceleration measurement	130

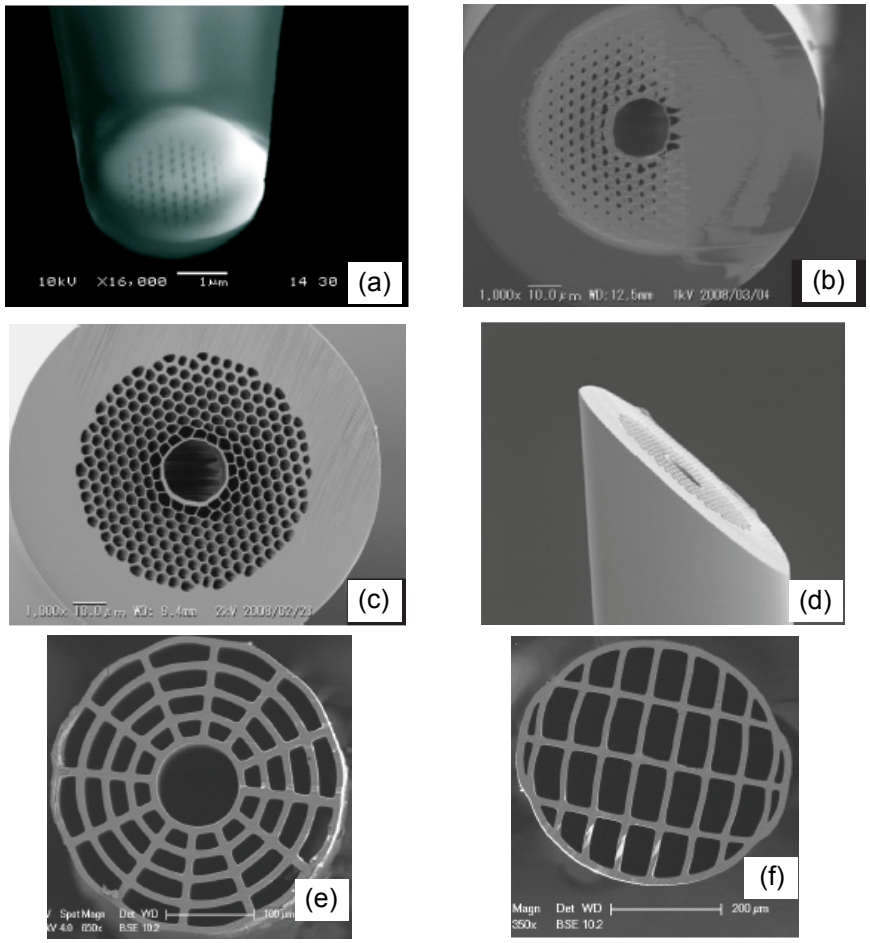

Figure 13: High-quality FIB cleaving of glass and polymer optical fibers at different angles. (a) SEM image of a cleaved PCF with a diameter of 3.5 µm [132]; SEM images of PCF endfacets cleaved by FIB (b) rough and (c) fine milling [133]; (d) SEM image of a PCF cleaved at 45^o [134]; SEM images of the cleaved endfacets of (e) spider-web and (f) rectangular polymer porous fibers [137].

Bragg grating (FBG) (Fig. 14).

The FBG is a periodic perturbation of the core refractive index along the fiber axis, where the optical fiber is either single-mode or multimode. Due to its periodic nature, the FBG behaves as a selective mirror that reflects the light for specific wavelengths, while transmitting the remaining wavelengths. The reflected light is centered at the Bragg wavelength, which can be expressed as $\lambda_B = 2 * n_{eff} * \Lambda$, where n_{eff} is the effective refractive index of the propagating mode in the fiber core, and Λ is the grating period. The patterning of such a FBG in a GeO_2 doped optical

Table 6: **Summary of FIB-cleaved optical fibers**

Fiber material	Fiber diameter	FIB process parameters	Applications	Ref.
Silica	d = 33 µm	10 nA	Low-loss butt-coupling	131
Silica	d = 3.5 µm	Ga, 30 kV, 280 pA	Microfluidics, Biophotonics	132
Silica	d = 115 µm	Ga, 25 kV, 6.4 nA/0.25 nA, 8 hours	Gas sensing	134
Silica	d_1 = 8.5 µm cleaved at 30^o d_2 = 3.5 µm cleaved at 45^o d_3 = 1 µm cleaved at 40^o	50 pA - 5 nA	Biological and chemical sensing	135
Polymer	d = 110 µm	30 kV, 20 nA/7 nA/5 nA	Low-loss butt-coupling	136
Polymer	d = 400 µm	Ga, 30 kV, 21 nA, 17.5 hours	Low-loss butt-coupling	137

fiber was first reported by Hill et al. in 1978 using an Argon-ion laser radiation [191]. Since then, FBGs have also been fabricated using a CO_2 laser [192], a phase mask in combination with either UV lithography [193] or a femtosecond laser [194, 195].

In general, the gratings inscribed in conventional optical fibers have weak index modulation, and thus a grating length of few millimeters is necessary to ensure strong modulation of the refractive index. Moreover, standard fibers are quite large compared to the needs of modern applications at the nanoscale. For this purpose, various micro- and nanofiber geometries, including fiber tapers, tip-polished fibers, side-polished fibers, and D-shaped fibers have been used to fabricate gratings in the core [196–201]. These fibers provide more compactness and mechanical robustness, and have stronger near-field interaction with surrounding medium, which allows relatively shorter gratings to be inscribed. The grating length can be further reduced by using FIB machining, to mill periodic nano-grooves by precisely controlling the size and the shape of each notch. The FIB milling technique has usually been applied on one of the aforementioned fiber geometries in order to get easy access to the fiber core and significantly reduce the milling time. In this section, we present a couple of applications of the FIB technology for fabricating fiber gratings.

By and large, FBGs have been fabricated on both tapered fiber tips [138–142] and the waist of biconical tapers [143–146]. In particular, a ∼12 µm-long Bragg grating was milled in a single-mode fiber tip with a diameter of 5.4 µm for temperature sensing (Fig. 15(a)) [141]. The FBG sensor was composed of 11 ∼1.6 µm-deep and ∼0.6 µm-long notches with a period of 1.1 µm.

Furthermore, Kou et al. experimentally demonstrated a 36.6 µm-long FBG carved on a 6.5 µm-diameter fiber taper for temperature sensing [139]. Fig. 15(b) shows an SEM image of the fabricated FBG composed of 61-period and 200 nm-deep grooves, where the grating period is 600 nm. In contrast, Ding et al. reported a ∼10 µm-long FBG milled in a ∼1.34 µm-diameter biconical tapered single-mode fiber for sensing applications (Fig. 15(c)) [145]. 30 kV accelerating voltage and 93 pA probe current were used to carve 20-biconcave notches with a period of ∼506 nm. The same research group also presented a phase-shifted FBG for 3D light confinement [144]. Recently, a grating structure consisting of 30 µm-long and 20 µm-deep 20 grooves, was also patterned on a graded-index multimode fiber for refractive index sensing [146]. Fig. 15(d) shows an SEM image of the milled structure, where the grating period is 1050 nm.

FIB machining was also used to integrate Bragg gratings within high Q-factor cavities [147–149]. Nayak et al. milled a grating mirror in a 560 nm-diameter silica fiber probe using a 10 pA beam current at 30 kV [147]. Each groove depth and width were measured as ∼100 nm and ∼150 nm, respectively, while the grating period was 360 nm (Fig. 16(a)). Later, a similar FIB-milled FBG was reported by Schell et al., where the groove depth was 45 nm and the pitch was 300 nm (Fig. 16(b)) [148]. More recently, ultra-high resolution (∼1 nm) He ion beam was used to mill a Bragg grating with a much higher Q-factor [149]. The patterned grating was composed of 640-grooves with a depth of 30 nm, and a pitch of 320 nm (Fig. 16(c)).

On top of fiber tapers, gratings have also been carved on D-shaped fibers using FIB milling. In particular, Yan et al. used FIB to pattern a metallic grating on the side surface of a D-shaped fiber (Fig. 17(a)) [150]. The polished surface, which was ∼6 µm away from the core, was first coated with an Au layer of 20 nm. A 38 µm-long grating was subsequently milled in the metal using a 100 pA beam current. The grating period was 485 nm, while the duty cycle was 50%. An SEM image of the fabricated metallic grating is illustrated in Fig. 17(b). It is worth mentioning that besides FIB milling, FIB implantation was also used to create fiber gratings [143].

The dimensions and the FIB process parameters used for the fabrication of the aforementioned fiber micrograting are summarized in Table 7.

4.7. Microcavities

Typical fiber-integrated Fabry–Perot resonators (FPR) are usually fabricated by cut air-slots penetrating the fiber core, thus enabling the formation of standing waves inside the cavity. Due to their simple structure, versatility, high sensitivity and linear response, fiber-

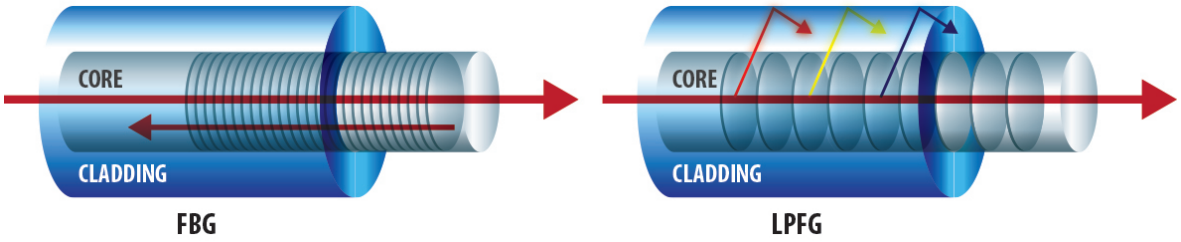

Figure 14: Schematic illustration of FBG and LPFG.

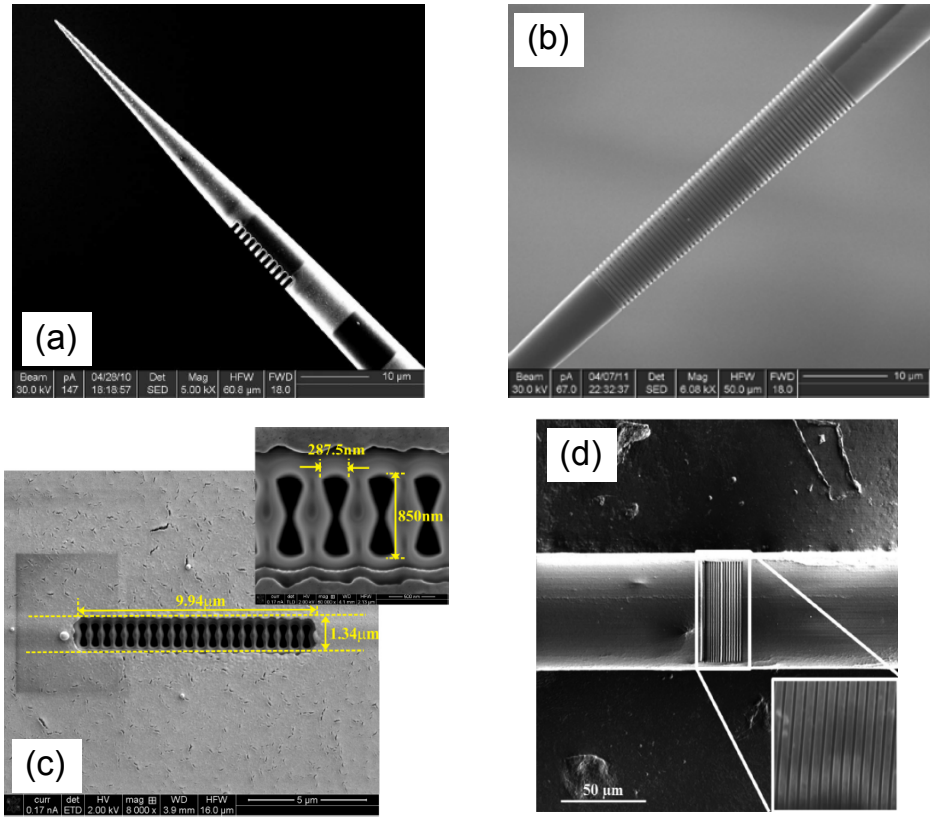

Figure 15: Fiber micrograting FIB-milled in tapered fiber tips and biconical fiber tapers. (a) SEM image of a 12 µm-long FBG composed of 11 notches [141]; (b) FIB image of a 36.6 µm-long FBG with a grating period of 600 nm [139]; (c) SEM image of a FBG milled in a biconical tapered fiber (partly embedded in the polymer) [145]; (d) SEM image of a fiber grating with a period of 1050 nm [146].

optic FPRs have been widely used in a variety of sensing applications for the measurement of various parameters such as pressure, strain, temperature, water salinity and refractive index [168, 202–209]. The free spectral range (FSR) of a FPR is inversely proportional to the cavity length: $FSR_\lambda = \lambda^2/(2 * n * L)$, where λ is the free space wavelength, n is the refractive index within the cavity, and L is the cavity length. Therefore, FPRs with small cavities become attractive due to their compactness, large FSR and high sensitivity. Very short cavities or micro-cavities can be fabricated using femtosecond (fs) laser micromachining and FIB milling. The former technique usually does not provide desirable smoothness of reflective surfaces inside the cavity resulting in poor reflectivity and fringe contrasts. Moreover, the fs laser machined cavity lengths are still in the order of tens of micrometers. In contrast, FIB milling allows the creation of ultra-short micro-cavities with high-quality surfaces. Here, we review several applications of the FIB milling technique for fabricating fiber microcavities.

In 2014, Wieduwilt et al. used FIB technology to fabricate a compact fiber refractive index sensor

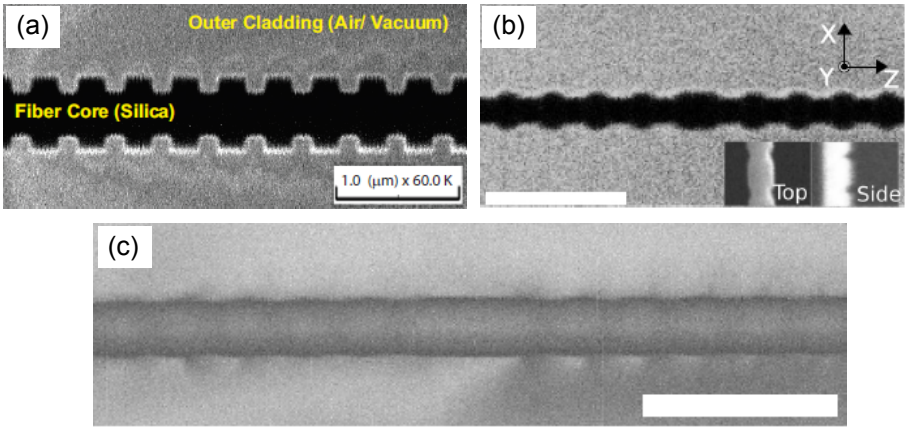

Figure 16: Scanning ion microscopy images of optical cavities integrated with FBGs using Ga and He FIB machining: (a) the groove depth, the groove width and the grating period are ∼100 nm, ∼150 nm, and 360 nm, respectively [147]; (b) the groove depth and the pitch are 45 nm and 300 nm, respectively [148]; (c) the groove depth and the pitch are 30 nm and 320 nm, respectively [149]. The scale bar is 1 µm.

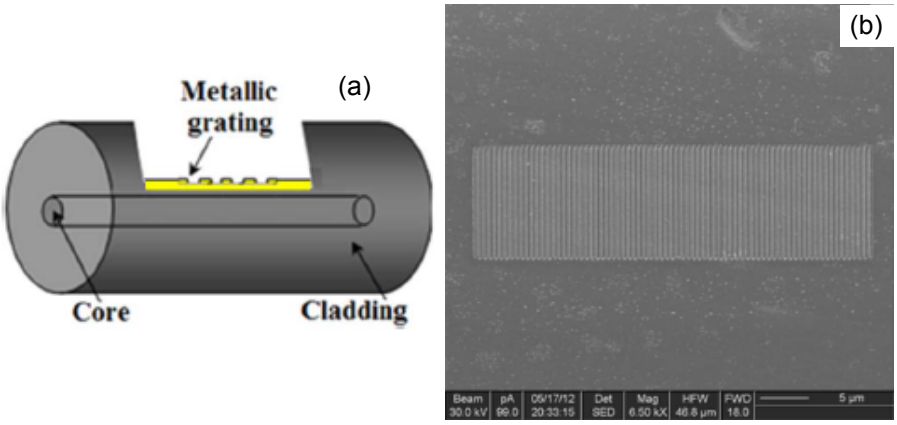

Figure 17: Metallic grating carved on a D-shaped fiber using FIB machining. (a) Schematic illustration and (b) SEM image of a 38.8 µm-long grating [150].

[151]. A beam current of 10 nA was used to mill a 24.85 µm-long cavity (Fig. 18(a-b)). The resonator walls were additionally coated with a hafnium oxide (HfO_2) layer of 190 nm to boost the reflectivity. FIB milling also enabled to create ultra-small FP cavities in tapered fibers for sensing applications. In particular, two different 5 µm-long and 2.8 µm-long cavities were milled in 10 µm-diameter fiber tapers using a beam current of 600 pA (Fig. 18(c)) [152]. The total milling time for each cavity was about 18 min. After the milling process, the fiber tip was cleaved by FIB at an angle of 45^o to reduce undesired reflections. Similar cavity structures of different lengths defined on fiber tapers were also presented in [153–158].

Furthermore, a side aligned optical fiber interferometer was experimentally demonstrated by Sun et al. using FIB milling [159]. A high beam current of 50 nA at 30 kV was used to remove huge volume of the fiber material to create a high aspect-ratio (∼20:1) cavity for sensing. Next, a 3 nA ion beam current was used to carve a 10 µm × 10 µm reflective mirror with a 45^o inclined angle to the fiber core at the center of the fiber tip to direct the core guided mode to the side of the fiber (Fig. 18(d)). The beam dwell time was fixed at 255 µs. FIB machining was also used to fabricate optical bottle microresonators (BMRs) to excite selected whispering gallery modes (Fig. 18(e)) [160].

It is worth noting that in most cases, the fabrication of cavity structures is a two-step process: a high beam current is first used for rough milling, and then a lower current is used to polish the sidewalls of the drilled cavity. This enables to reduce the total milling time and produce smoother reflecting surfaces.

The dimensions and the FIB process parameters used for the fabrication of the aforementioned fiber micrcavities are summarized in Table 8.

Table 7: **Summary of FIB-fabricated fiber micrograting (w - notch width, l - notch length, h - notch depth, Λ - grating period, L_g - grating length, n - number of periods)**

Structure	Dimensions	FIB process parameters	Applications	Ref.
Grating	L_g = 31 µm, Λ = 1 µm, w = 0.5 µm, l = 10 µm, h = 3 µm	Ga, 30 kV, 300 pA, 30 min	Sensing	143
Metal-dielectric-hybrid grating	L_g = 10 µm, Λ = 578 nm, n = 17	Ga, 30 kV, 58 pA	Refractive index sensing	138
FBG	L_g = 36.6 µm, Λ = 600 nm, n = 61, h = 200 nm	Ga	Temperature sensing	139
FBG	L_g = 518 µm, Λ = 576 nm, n = 61, h = 100 nm	Ga, 30 kV, 70 pA	Refractive index sensing	140
FBG	Λ = 467 nm, n = 20, w = 156.2 nm, l = 718.7 nm	Ga, 30 kV, 93 pA	Sensing	144
FBG	L_g = 9.4 µm, Λ = 506 nm, n = 20, w = 287.5 nm, l = 850 nm	Ga, 30 kV, 93 pA	Sensing	145
FBG	L_g = 12 µm, Λ = 1.1 µm, n = 11, w = 0.6 µm, h = 1.6 µm	Ga	Temperature sensing	141
FBG	Λ = 360 nm, w = 150 nm, h = 100 nm	Ga, 30 kV, 10 pA	Quantum information technology	147
Metallic grating	L_g = 38.8 µm, Λ = 485 nm, w = 0.5 µm, l = 10 µm, h = 3 µm	Ga, 30 kV, 100 pA	Refractive index sensing	150
FBG	L_g = 27 µm, Λ = 540 nm, n = 50, w = 270 nm	115 pA, 50 min	Temperature sensing	142
FBG	Λ = 300 nm, n = 160, h = 45 nm	Ga, 30 kV, 93 pA	Single photon sources	148
FBG	Λ = 320 nm, n = 160, h = 30 nm	He, 1 pA	Quantum information devices	149
FBG	L_g = 30 µm, Λ = 1050 nm, n = 20, h = 20 µm	Ga	Refractive index sensing	146

Table 8: **Summary of FIB-fabricated fiber microcavities (w - cavity width, l - cavity length, h - cavity depth)**

Structure	Dimensions	FIB process parameters	Applications	Ref.
FP cavity	l = 4.4 µm, h = 5 µm	Ga, 30 kV, 291 pA	Temp. sensing	153
FP cavity	l = 3.5 µm, h = 2.94 µm	Ga, 30 kV, 288 pA	Refractive index sensing	154
FP cavity	l = 74 µm	30 kV, 11.5 nA	Temp. and water salinity sensing	156
FP cavity	w = 10 µm, l = 25 µm, h = 32 µm	Ga, 20 nA, 20 min	Refractive index sensing	155
FP cavity	w = 5 µm, l = 50 µm, h = 6 µm	Ga, 30 kV, 2.8 nA	Exciting whispering gallery modes	160
FP cavity	w = 20 µm, l = 100 µm, h = 450 µm	30 kV, 50 nA	Sensing	159
FP cavities	l_1 = 167 µm, l_2 = 1025 µm	1 nA, 80 min	Temp. and vibration sensing	158
FP cavity	l = 24.85 µm, h = 18 µm	10 nA	Refractive index sensing	151
FP cavities	l_1 = 53 µm, l_2 = 55 µm	Ga, 30 kV, 1-3 nA	Temp. and refractive index sensing	158
FP cavity	l = 100 µm, h = 80 µm	Ga, 25 kV, 6.4 nA, 70 hours	Refractive index sensing	157
FP cavities	l_1 = 5 µm, l_2 = 2.8 µm, h = 5.1 µm	0.6 nA, 18 min	Refractive index sensing	152

4.8. Access holes and channels

Microstructured optical fibers (MOFs) are another type of fiber composed of a matrix of air-holes structured along the entire fiber length. In contrast to conventional optical fibers, where the refractive indices of the core and cladding are slight different, MOFs are made of one material. The air-holes in MOFs are usually arranged periodically forming a subgroup of MOFs known as photonic crystal fibers (PCFs). The unique microstructure and long interaction length between the guided light and the inserted sample (gas, liquid or polymer) enable the effective use of PCFs in sensing applications. The sample is usually filled into the fiber holes through one of tips, which complicates the further use of the fiber tip for light in- and out-coupling. Alternatively, the sample can be inserted through an access channel created in the fiber cladding, leaving the fiber endfacets free for optical access. FIB machining, which enables precise control of the depth and shape of an opening, has been effectively used to mill channels for lateral access to the longitudinal fiber air-holes without interfering with the fiber endfacet [161–169].

In particular, Cordeiro et al. used a FIB system to define side holes of different shapes for lateral access to the PCF air-holes [161]. The 28 µm-thick silica jacket of a 120 µm-diameter suspended-core PCF was initially etched by hydrofluoric (HF) acid to reduce the FIB milling time from 9 min to 130 sec for a 20 µm x 5 µm hole. After the process parameter optimization, a 30 kV accelerating voltage and a 20 nA beam current were used to mill rectangular and circular holes without disturbing the fiber core (Fig. 19(a-b)). Similar types

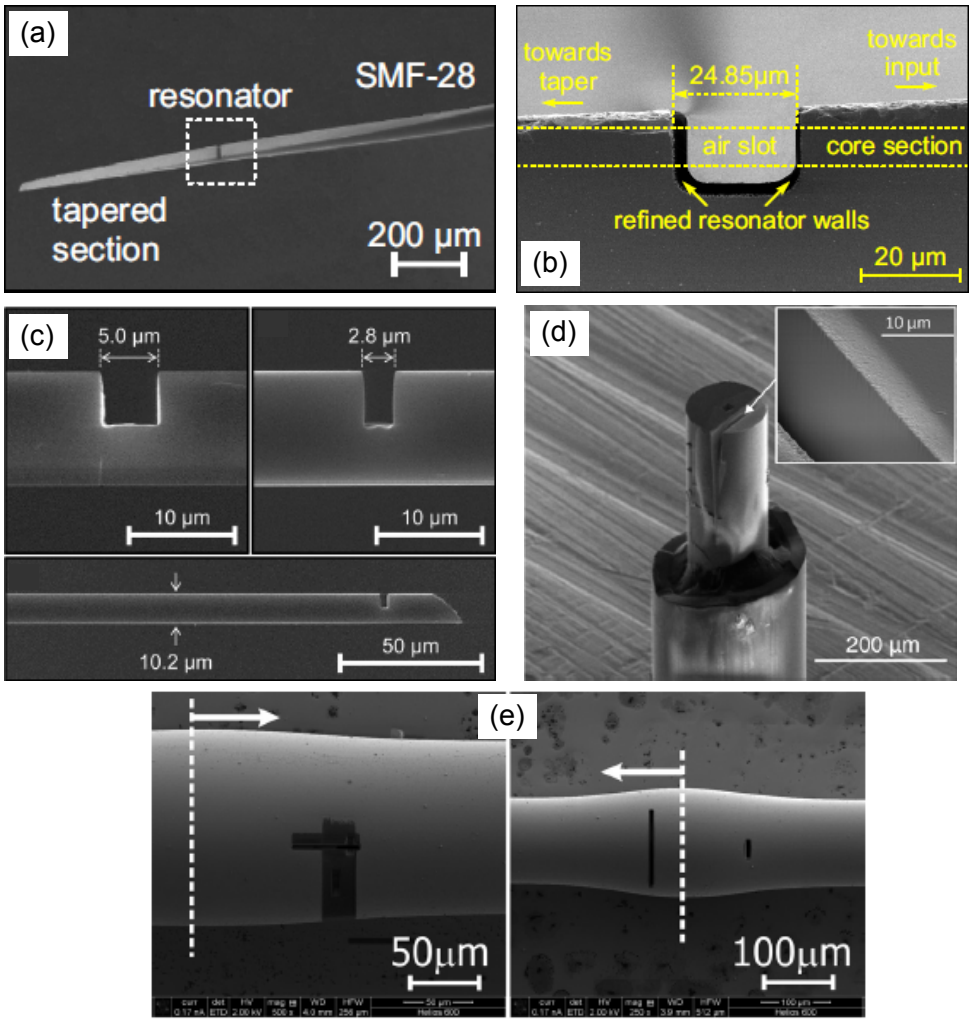

Figure 18: SEM images of microcavities carved in optical fibers using FIB machining. (a-b) a milled and refined microcavity [151]; (c) FP cavities of different lengths [152]; (d) a fiber-side interferometer [159]; (e) bottle microresonators: (left) the horizontal groove is 5 µm-wide, 50 µm-long and 6 µm-deep; (right) the width, length, and depth for the left and right grooves are 5 µm, 109 µm, 6 µm and 5.5 µm, 27.5 µm, 6 µm, respectively [160].

of side holes were also experimentally demonstrated by Martelli et al. for a four-ring solid-core PCF and for a six-hole step-index fiber [162].

Furthermore, FIB was employed to create an access hole directly into the core of a fiber. In particular, Warren-Smith et al. used an exposed-core MOF for fabricating two different types of cavity structures for chemical and biological sensing applications [166]. The exposed-core MOF was first made by drilling three holes into the center of a fused silica glass rod. The core was subsequently exposed by cutting a slot into one of the holes using a diamond blade (Fig. 19(c)). The exposed-core MOF was then spliced to a single-mode fiber. One of the milled cavities with a length of 34.6 µm, cut through the core penetrating into the fiber holes (Fig. 19(d)), while the other 28.9 µm-long cavity structure was a shallow rectangle milled into the center of the core (Fig. 19(e)). The total milling took around 3 hours and 12 min for the long (deep) cavity and the short (shallow) cavity, respectively.

FIB micromachining was also used to mill micro-channels in the facet of a fiber. A beam current of 20 nA at 30 kV was used to precisely mill two 43 µm x 30 µm channels 50 µm-deep into the cladding of a hollow-core fiber (Fig. 19(f-g)) [169]. This enables direct access for a sample (gas or liquid) to the hollow core even though the fiber is spliced to a solid-core fiber. Similar channels were carved on the endfacet of a solid-core PCF for selective infiltration (Fig. 19(h-i)) [163]. After the milling of the channels, the PCF was spliced to a standard single-mode fiber. In this case, the PCF holes connected to the channels would be filled if the spliced fiber was immersed into a fluid. Furthermore, Gomes

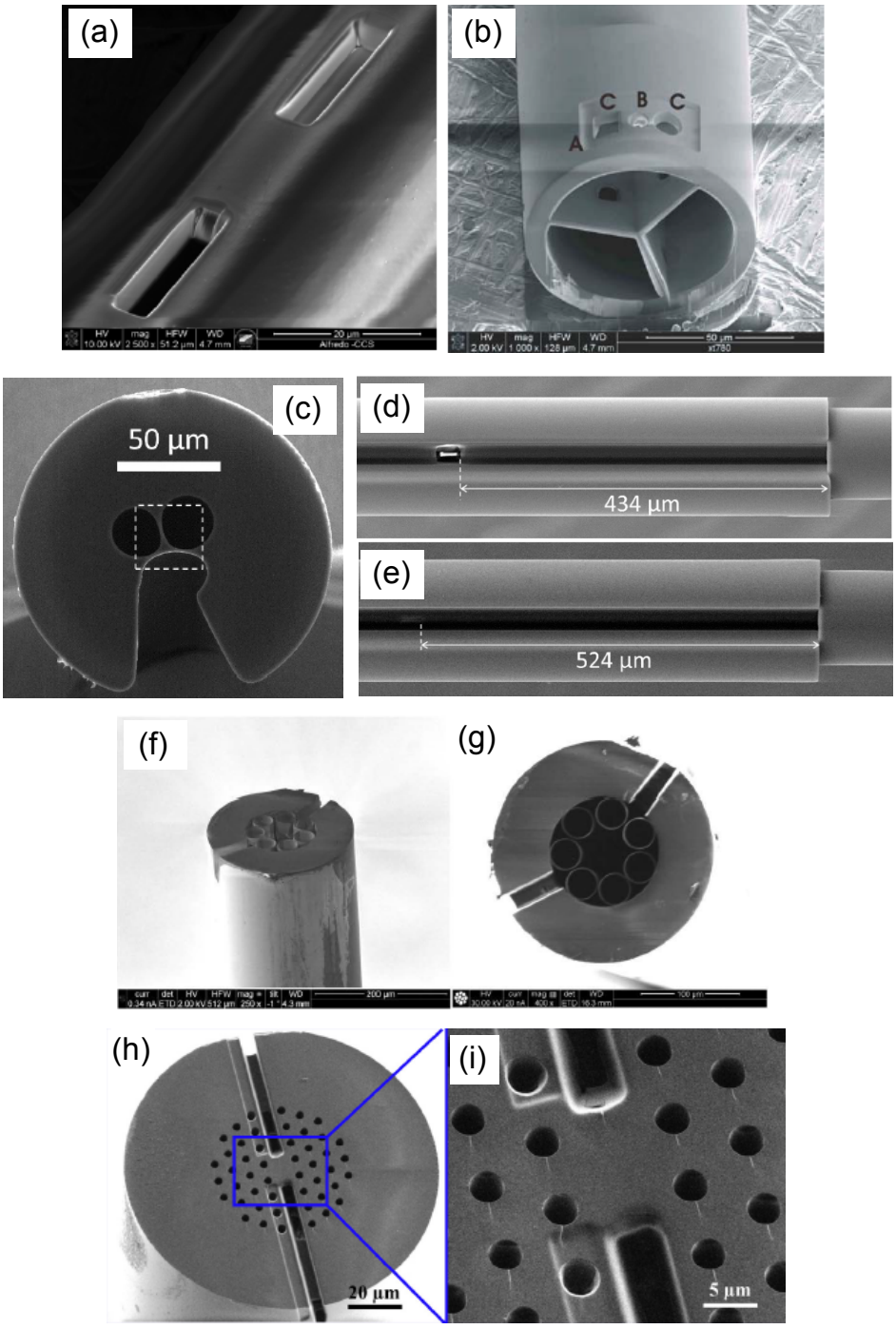

Figure 19: SEM images of FIB-milled channels and holes for lateral access to the longitudinal fiber air-holes. (a-b) rectangular and circular holes milled in the PCF cladding [161]; (c) an exposed-core fiber (ECF), (d) a FP cavity that cut through the ECF core penetrating into the fiber holes and (e) a shallow FP cavity [166]; (f) side view and (g) top view of two channels of 43 µm x 30 µm milled in a hollow-core fiber [169]; (h-i) 5 µm-deep and 5 µm-wide channels milled in a solid-core PCF [163].

et al. reported a sensor composed of a caterpillar-like MOF spliced to a single-mode optical fiber, where the spliced endfacet contains FIB-milled transversal microfluidic channels [165].

The dimensions and the FIB process parameters used for the fabrication of the aforementioned access holes and channels are summarized in Table 9.

Table 9: **Summary of FIB-milled access holes and channels (w - channel width, l - channel length, h - channel depth, d - hole diameter)**

Structure	Dimensions	FIB process parameters	Applications	Ref.
Rectangular hole Circular hole	w = 5 µm, l = 20 µm d = 8 µm	Ga, 30 kV, 20 nA, 2.2 min	Sensing	161
Circular holes	d = 12 µm, h = 68 µm d = 15 µm, h = 7 µm	Ga, 20 nA	Sensing	162
Rectangular channel	w = 5 µm, h = 5 µm	Ga, 30 kV, 20 nA	Sensing	163
Square hole	w = l = 28 µm, h = 125 µm	Ga, 30 kV, 50 nA	Sensing	164
Channel	-	-	Sensing	165
1. Deep cavity 2. Shallow cavity	1. l = 34.6 µm 2. w = 2.5 µm, l = 28.9 µm	1. 2 nA, 3 hours 2. 0.63 nA, 12 min	Sensing	166
Rectangular hole	h = 37.5 µm	Ga, 30 kV, 20 nA	Sensing	167
Square channel	w = l = 15 µm	30 kV, 65 nA, 8 min	Sensing	168
Rectangular channel	w = 30 µm, l = 43 µm, h = 50 µm	Ga, 30 kV, 2 nA, 30 min	Sensing	169

5. Conclusions

FIB machining plays a vital role in nano-manufacturing due to its sub-10nm resolution, flexibility, and high-precision fabrication of sub-micrometer devices. In contrast to other conventional processing methods, this powerful and versatile technique offers valuable advantages such as the capability of direct patterning on both conventional planar substrates and irregular (curved) surfaces, as well as the ability to precisely realize any geometry on any type of material. On the other hand, the FIB technology also has obvious drawbacks, including high manufacturing cost, high vacuum conditions, and low throughput, which practically limit its application in mass production of nanostructures. However, this technique can still be effectively utilized for rapid prototyping of various structures.

In this paper, we have presented a general overview of the FIB technology and its typical applications in manufacturing of fiber-optic devices for diverse applications. First, the overview of a FIB system and its fundamental functions, including milling, deposition, implantation, and imaging, are discussed. Subsequently, the capabilities of FIB machining for the fabrication of various NSOM fiber probes, fiber cantilevers, beam-shaping structures, plasmonic nano-arrays, access holes and channels, micrograting, and microcavities are demonstrated. Moreover, the FIB milling for fiber tip smooth cleaving is presented.

In general, a spot size as small as 5 nm can be achieved by Ga FIB systems at very low ion beam currents (∼1 pA). However, the currently developing He gas ion sources could practically enable further reduction of the beam diameter leading to substantial enhancement of the spatial resolution. Therefore, He FIB systems would pave the way for FIB technology to produce ultra-small features.

The further automation of the FIB systems to enable better control of the hardware and software, as well as faster alignments of an optical fiber with respect to the ion column would substantially increase the processing throughput simplifying the incorporation with other fabrication techniques.

Currently, the precursor gases in commercial FIB systems are usually limited to Pt, W, Al and Au. Introducing more precursor gases for depositing diverse metals and significantly reducing the content of Carbon in the deposited metals would also facilitate the manufacturing of various devices, as well as improve the performances of the fabricated devices.

Since FIB technology can practically utilized for both top-down and bottom-up manufacturing, it has a great potential to be effectively used for the chemical growth of functional materials on the fiber surfaces similar to widely used self-assembly and chemical vapor deposition techniques.

References

[1] Luesakul U, Komenek S, Puthong S and Muangsin N 2016 *Carbohydr. Polym.* **153** 435–444

[2] Li Y, Yang J, Zhou Y, Zhao N, Zeng W and Wang W 2017 *Colloids Surf., A* **512** 93–100

[3] Layani M, Wang X and Magdassi S 2018 *Adv. Mater.* **30** 1706344

[4] Wang K, Guan J, Mi F, Chen J, Yin H, Wang J and Yu Q 2015 *Mater. Lett.* **161** 317–320

[5] Manawi Y M, Ihsanullah, Samara A, Al-Ansari T and Atieh M A 2018 *Materials* **11** 1–36

[6] Zhou J, Zeng Q, Lv D, Sun L, Niu L, Fu W, Liu F, Shen Z, Jin C and Liu Z 2015 *Nano Lett.* **15** 6400–6405

[7] Meng X, Wang X, Geng D, Ozgit-Akgun C, Schneider N and Elam J W 2017 *Mater. Horiz.* **4**(2) 133–154

[8] Kim H G and Lee H B R 2017 *Chem. Mater.* **29** 3809–3826

[9] Yao Y, Zhang L, Leydecker T and Samorì P 2018 *J. Am. Chem. Soc.* **140** 6984–6990

[10] Yang D, Ramu A G, Lee Y, Kim S, Jeon H, V E S, Al-Mohaimeed A M, Al-onazi W A, saad Algarni T and Choi D 2021 *J. King Saud Univ. Sci.* **33** 101397

[11] Altissimo M 2010 *Biomicrofluidics* **4** 026503

[12] Chen Y 2015 *Microelectron. Eng.* **135** 57–72

[13] Gierak J 2009 *Semicond. Sci. Technol.* **24** 043001

[14] Kim C S, Ahn S H and Jang D Y 2012 *Vacuum* **86** 1014–1035

[15] Li P, Chen S, Dai H, Yang Z, Chen Z, Wang Y, Chen Y, Peng W, Shan W and Duan H 2021 *Nanoscale* **13** 1529–1565

[16] Ding G, Jin Q, Chen Q, Hu Z and Liu J 2015 *Nanoscale Res. Lett.* **10** 1–10

[17] Kikuchi T, Nishinaga O, Natsui S and Suzuki R O 2015 *Appl. Surf. Sci.* **341** 19–27

[18] Zhang Z, Luo J, Song M and Yu H 2015 *Appl. Phys. Lett.* **107** 241904

[19] Valsecchi C, Gomez Armas L E and Weber de Menezes J 2019 *Sensors* **19** 1–12

[20] Deng Z, Yang Q, Chen F, Meng X, Bian H, Yong J, Shan C and Hou X 2015 *Opt. Lett.* **40** 1928–1931

[21] Worts N, Jones J and Squier J 2019 *Opt. Commun.* **430** 352–357

[22] Yue W, Wang Z, Yang Y, Chen L, Syed A, Wong K and Wang X 2012 *J. Micromech. Microeng.* **22** 125007

[23] Tian W C, Ho Y H, Chen C H and Kuo C Y 2013 *Sensors* **13** 865–874

[24] Petti L, Capasso R, Rippa M, Pannico M, La Manna P, Peluso G, Calarco A, Bobeico E and Musto P 2016 *Vib. Spectrosc.* **82** 22–30

[25] Vinje J, Beckwith K S and Sikorski P 2020 *J. Microelectromech. Syst.* **29** 160–169

[26] Reyntjens S and Puers R 2001 *J. Micromech. Microeng.* **11** 287–300

[27] Langford R M, Nellen P M, Gierak J and Fu Y 2007 *MRS Bull.* **32** 417–423

[28] Sloyan K, Melkonyan H and Dahlem M S 2020 *Int. J. Adv. Manuf. Technol.* **107** 4469–4480

[29] Tao T, Wilkinson W and Melngailis J 1991 *J. Vac. Sci. Technol., B: Microelectron. Nanometer Struct. Process., Meas., Phenom.* **9** 162–164

[30] Harriott L R, Wagner A and Fritz F 1986 *J. Vac. Sci. Technol., B: Microelectron. Process. Phenom.* **4** 181–184

[31] Abramo M T and Hahn L L 1996 *Microelectron. Reliab.* **36** 1775–1778

[32] Volinsky A A, Rice L, Qin W and Theodore N D 2004 *Microelectron. Eng.* **75** 3–11

[33] Nikawa K 1991 *J. Vac. Sci. Technol., B: Microelectron. Nanometer Struct. Process. Meas. Phenom.* **9** 2566–2577

[34] Mayer J, Giannuzzi L A, Kamino T and Michael J 2007 *MRS Bull.* **32** 400–407

[35] Kato N I 2004 *Microscopy* **53** 451–458

[36] Langford R M and Petford-Long A K 2001 *J. Vac. Sci. Technol. A* **19** 2186–2193

[37] Langford R M 2006 *Microsc. Res. Tech.* **69** 538–549

[38] Hutchinson C, Hackenberg R and Shiflet G 2003 *Ultramicroscopy* **94** 37–48

[39] Ünlü N 2008 *Mater. Charact.* **59** 547–553

[40] Li F, Li S, Tong H, Xu H and Wang Y 2020 *Materials* **13** 1–9

[41] Freeman D, Madden S and Luther-Davies B 2005 *Opt. Express* **13** 3079–3086

[42] Kim Y K, Danner A J, Raftery J J and Choquette K D 2005 *IEEE J. Sel. Top. Quantum Electron.* **11** 1292–1298

[43] Yao W, Liu S, Liao H, Li Z, Sun C, Chen J and Gong Q 2015 *Nano Lett.* **15** 3115–3121

[44] Maleki A, Vo T P, Hautin A, Downes J E, Coutts D W and Dawes J M 2016 *Plasmonics* **11** 365–372

[45] Lunt A J G and Korsunsky A M 2015 *Surf. Coat. Technol.* **283** 373–388

[46] Ageev O A, Kolomiytsev A S, Bykov A V, Smirnov V A and Kots I N 2015 *Microelectron. Reliab.* **55** 2131–2134

[47] Knittel P, Hibst N, Mizaikoff B, Strehle S and Kranz C 2017 *Ultramicroscopy* **179** 24–32

[48] Gierak J, Mazarov P, Bruchhaus L, Jede R and Bischoff L 2018 *J. Vac. Sci. Technol. B* **36** 06J101

[49] Bischoff L, Klingner N, Mazarov P, Pilz W and Meyer F 2020 *J. Vac. Sci. Technol. B* **38** 042801

[50] Kellogg S, Schampers R, Zhang S, Graupera A, Miller T, Laur W D and Dirriwachter A 2010 *Microsc. Microanal.* **16** 222–223

[51] Hrncir T, Delobbe A, Salord O, Lopour F, Zadrazil M and Sudraud P 2012 Novel plasma fib/sem for high speed failure analysis and real time imaging of large volume removal *Proc. 38th int. symp. test. failure analys.*

[52] Garnier A, Filoni G, Hrnčíř T and Hladík L 2015 *Microelectron. Reliab.* **55** 2135–2141

[53] Joy D C 2013 *Helium ion microscopy: principles and applications* 1st ed (New York, USA: Springer)

[54] Hlawacek G and Gölzhäuser A 2016 *Helium ion microscopy* 1st ed (Springer)

[55] Bruchhaus L, Mazarov P, Bischoff L, Gierak J, Wieck A D and Hövel H 2017 *Appl. Phys. Rev.* **4** 011302

[56] Jain I P and Agarwal G 2011 *Surf. Sci. Rep.* **66** 77–172

[57] Frey L, Lehrer C and Ryssel H 2003 *Appl. Phys. A* **76** 1017–1023

[58] Beuer S, Rommel M, Lehrer C, Platzgummer E, Kvasnica S, Bauer A J and Ryssel H 2007 *Microelectron. Eng.* **84** 810–813

[59] Chyr I and Steckl A J 2001 *J. Vac. Sci. Technol., B: Microelectron. Nanometer Struct. Process. Meas. Phenom.* **19** 2547–2550

[60] Fu X L, Li P G, Jin A Z, Chen L M, Yang H F, Li L H, Tang W H and Cui Z 2005 *Microelectron. Eng.* **78-79** 29–33

[61] Hellborg R, Whitlow H J and Zhang Y 2010 *Ion beams in nanoscience and technology* 1st ed (Springer)

[62] Fu Y and Bryan N K A 2005 *Appl. Phys. B* **80** 581–585

[63] Boxer S G, Kraft M L and Weber P K 2009 *Annu. Rev. Biophys.* **38** 53–74

[64] Baer D R, Gaspar D J, Nachimuthu P, Techane S D and Castner D G 2010 *Anal. Bioanal. Chem.* **396** 983–1002

[65] Cusano A, Consales M, Crescitelli A and Ricciardi A 2015 *Lab-on-fiber technology* 1st ed vol 56 (Springer)

[66] Pisco M and Cusano A 2020 *Sensors* **20** 1–20

[67] Estevez M C, Alvarez M and Lechuga L M 2012 *Laser Photonics Rev.* **6** 463–487

[68] Temiz Y, Lovchik R D, Kaigala G V and Delamarche E 2015 *Microelectron. Eng.* **132** 156–175

[69] Bao Q, Zhang H, Wang Y, Ni Z, Yan Y, Shen Z X, Loh K P and Tang D Y 2009 *Adv. Funct. Mater.* **19** 3077–3083

[70] Wu K, Chen B, Zhang X, Zhang S, Guo C, Li C, Xiao P, Wang J, Zhou L, Zou W and Chen J 2018 *Opt. Commun.* **406** 214–229

[71] Sciacca B and Monro T M 2014 *Langmuir* **30** 946–954

[72] Credi C, Bibikova O, Dallari C, Tiribilli B, Ratto F, Centi S, Pini R, Artyushenko V, Cicchi R and Pavone F S 2020 *J. Mater. Chem. B* **8**(8) 1629–1639

[73] Shin J, Bosworth B T and Foster M A 2016 *Opt. Lett.* **41** 886–889

[74] Vaiano P, Carotenuto B, Pisco M, Ricciardi A, Quero G, Consales M, Crescitelli A, Esposito E and Cusano A 2016 *Laser Photonics Rev.* **10** 922–961

[75] Xiong Y and Xu F 2020 *Adv. Photonics* **2** 1–24

[76] Muranishi M, Sato K, Hosaka S, Kikukawa A, Shintani T and Ito K 1997 *Jap. J. Appl. Phys.* **36** L942–L944

[77] Pilevar S, Edinger K, Atia W, Smolyaninov I and Davis C 1998 *Appl. Phys. Lett.* **72** 3133–3135

[78] Veerman J A, Otter A M, Kuipers L and Van Hulst N F 1998 *Appl. Phys. Lett.* **72** 3115–3117

[79] Lacoste T, Huser T, Prioli R and Heinzelmann H 1998 *Ultramicroscopy* **71** 333–340

[80] Zhang Y, Dhawan A and Vo-Dinh T 2010 *Nanoscale Res. Lett.* **6** 1–6

[81] Neumann L, Pang Y, Houyou A, Juan M L, Gordon R and Van Hulst N F 2011 *Nano Lett.* **11** 355–360

[82] Spajer M, Parent G, Bainier C and Charraut D 2001 *J. Microsc.* **202** 45–49

[83] Fang J Y, Tien C H and Shieh H P D 2007 *Opt. Express* **15** 14619–14628

[84] Mivelle M, Ibrahim I A, Baida F, Burr G W, Nedeljkovic D, Charraut D, Rauch J Y, Salut R and Grosjean T 2010 *Opt. Express* **18** 15964–15974

[85] Mivelle M, Van Zanten T S, Neumann L, Van Hulst N F and Garcia-Parajo M F 2012 *Nano Lett.* **12** 5972–5978

[86] Kim J B and Chang W S 2016 *Microelectron. Eng.* **151** 24–29

[87] Sloyan K, Melkonyan H, Chiesa M and Dahlem M S 2019 Fabrication of near-field optical fiber probes through focused ion beam *CLEO* (Optical Society of America) p SM2L.3

[88] Smythe E J, Cubukcu E and Capasso F 2007 *Opt. Express* **15** 7439–7447

[89] Dhawan A and Muth J F 2008 *Mater. Sci. Eng., B* **149** 237–241

[90] Dhawan A, Muth J F, Leonard D N, Gerhold M D, Gleeson J, Vo-Dinh T and Russell P E 2008 *J. Vac. Sci. Technol. B: Microelectron. Nanometer Struct. Process. Meas. Phenom.* **26** 2168–2173

[91] Dhawan A, Gerhold M D and Muth J F 2008 *IEEE Sens. J.* **8** 942–950

[92] Dhawan A, Gerhold M, Madison A, Fowlkes J, Russell P E, Vo-Dinh T and Leonard D N 2009 *Scanning* **31** 139–146

[93] Zhao Y, Zhou F, Xu F and Lu Y Q 2012 *IEEE Photonics J.* **4** 1288–1294

[94] Nguyen H, Sidiroglou F, Collins S F, Davis T J, Roberts A and Baxter G W 2013 *Appl. Phys. Lett.* **103** 193116

[95] Andrade G F S, Hayashi J G, Rahman M M, Salcedo W J, Cordeiro C M B and Brolo A G 2013 *Plasmonics* **8** 1113–1121

[96] Tian Y, Wu N, Zou X and Wang X 2013 Fiber optic ultrasound generator using periodic gold nanopattern fabricated by focused ion beam *Nondestruct. Charac. Composite Mater. Aerosp. Eng. Civil Infrastruc. Homeland Secur.* vol 8694 International Society for Optics and Photonics (SPIE) pp 546–552

[97] Principe M, Consales M, Micco A, Crescitelli A, Castaldi G, Esposito E, La Ferrara V, Cutolo A, Galdi V and Cusano A 2017 *Light: Sci. Appl.* **6** e16226

[98] Xomalis A, Demirtzioglou I, Plum E, Jung Y, Nalla V, Lacava C, MacDonald K F, Petropoulos P, Richardson D J and Zheludev N I 2018 *Nat. Commun.* **9** 1–7

[99] Kim H M, Uh M, Jeong D H, Lee H Y, Park J H and Lee S K 2019 *Sens. Actuators, B* **280** 183–191

[100] Kim H T and Yu M 2019 *Sci. Rep.* **9** 1–9

[101] Yang J, Ghimire I, Wu P C, Gurung S, Arndt C, Tsai D P and Lee H W H 2019 *Nanophotonics* **8** 443–449

[102] Schiappelli F, Kumar R, Prasciolu M, Cojoc D, Cabrini S, De Vittorio M, Visimberga G, Gerardino A, Degiorgio V and Di Fabrizio E 2004 *Microelectron. Eng.* **73-74** 397–404

[103] Cabrini S, Liberale C, Cojoc D, Carpentiero A, Prasciolu M, Mora S, Degiorgio V, De Angelis F and Di Fabrizio E 2006 *Microelectron. Eng.* **83** 804–807

[104] Minzioni P, Bragheri F, Liberale C, Di Fabrizio E and Cristiani I 2008 *IEEE J. Sel. Top. Quantum Electron.* **14** 151–157

[105] Chen W, Han W, Abeysinghe D C, Nelson R L and Zhan Q 2010 *J. Opt.* **13** 015003

[106] Kang S, Joe H E, Kim J, Jeong Y, Min B K and Oh K 2011 *Appl. Phys. Lett.* **98** 241103

[107] Liu Y, Stief F and Yu M 2013 *Opt. Lett.* **38** 721–723

[108] Guan C, Ding M, Shi J, Hua P, Wang P, Yuan L and Brambilla G 2014 *Opt. Express* **22** 18365–18371

[109] Berthelot J, Aćimović S S, Juan M L, Kreuzer M P, Renger J and Quidant R 2014 *Nat. Nanotechnol.* **9** 295–299

[110] Han J, Sparkes M and O'Neill W 2015 *Appl. Opt.* **54** 890–894

[111] Vayalamkuzhi P, Bhattacharya S, Eigenthaler U, Keskinbora K, Samlan C T, Hirscher M, Spatz J P and Viswanathan N K 2016 *Opt. Lett.* **41** 2133–2136

[112] Ribeiro R S R, Dahal P, Guerreiro A, Jorge P and Viegas J 2016 *Opt. Lett.* **41** 2137–2140

[113] Janeiro R, Flores R, Dahal P and Viegas J 2016 *Opt. Express* **24** 11611–11625

[114] Melkonyan H, Qubaisi K A, Sloyan K, Khilo A and Dahlem M S 2017 *Opt. Express* **25** 13035–13045

[115] Melkonyan H, Sloyan K, Twayana K, Moreira P and Dahlem M S 2017 *IEEE Photonics J.* **9** 1–9

[116] Ribeiro R S R, Dahal P, Guerreiro A, Jorge P A S and Viegas J 2017 *Sci. Rep.* **7** 1–14

[117] Kim H, Kim J, An H, Lee Y, Lee G Y, Na J, Park K, Lee S, Lee S Y, Lee B and Jeong Y 2017 *Opt. Express* **25** 30290–30303

[118] Sloyan K, Melkonyan H, Moreira P and Dahlem M S 2017 Optical fiber plasmonic lens for near-field focusing fabricated through focused ion beam *Advanced Fabrication Technologies for Micro/Nano Optics and Photonics X* vol 10115 (SPIE) pp 49 – 54

[119] Pisano F, Pisanello M, Sileo L, Qualtieri A, Sabatini B L, De Vittorio M and Pisanello F 2018 *Microelectron. Eng.* **195** 41–49

[120] Melkonyan H, Sloyan K, Odeh M, Almansouri I, Chiesa M and Dahlem M S 2019 *JPhys Photonics* **1** 025004

[121] Yu J, Fu C, Bai Z and Wang Y 2021 *J. Lightwave Technol.* **39** 1416–1422

[122] Iannuzzi D, Deladi S, Gadgil V J, Sanders R G P, Schreuders H and Elwenspoek M C 2006 *Appl. Phys. Lett.* **88** 053501

[123] Iannuzzi D, Deladi S, Berenschot J W, De Man S, Heeck K and Elwenspoek M C 2006 *Rev. Sci. Instrum.* **77** 106105

[124] Deladi S, Iannuzzi D, Gadgil V J, Schreuders H and Elwenspoek M C 2006 *J. Micromech. Microeng.* **16** 886–889

[125] Iannuzzi D, Heeck K, Slaman M, Man S D, Rector J H, Schreuders H, Berenschot J W, Gadgil V J, Sanders R G P, Elwenspoek M C and Deladi S 2007 *Meas. Sci. Technol.* **18** 3247–3252

[126] Alberts C J, Man S D, Berenschot J W, Gadgil V J, Elwenspoek M C and Iannuzzi D 2009 *Meas. Sci. Technol.* **20** 034005

[127] André R M, Pevec S, Becker M, Dellith J, Rothhardt M, Marques M B, Donlagic D, Bartelt H and Frazão O 2014 *Opt. Express* **22** 13102–13108

[128] Li J, Albri F, Sun J N, Miliar M M, Maier R R J, Hand D P and MacPherson W N 2014 *Meas. Sci. Technol.* **25** 035206

[129] Li J, Albri F, Maier R R J, Shu W, Sun J, Hand D P and MacPherson W N 2015 *IEEE Sens. J.* **15** 7221–7228

[130] Li J, Wang G Y, Sun J N, Maier R R J, Macpherson W N, Hand D P and Dong F Z 2017 *IEEE Photonics Technol. Lett.* **29** 1836–1839

[131] Fielding A J, Edinger K and Davis C C 1999 *J. Lightwave Technol.* **17** 1649–1656

[132] Gibson B C, Huntington S T, Rubanov S, Olivero P, Digweed-Lyytikäinen K, Canning J and Love J D 2005 *Opt. Express* **13** 9023–9028

[133] Li X, Pawłat J, Liang J, Xu G and Ueda T 2009 *Jon. J. Appl. Phys.* **48** 06FK05

[134] Li X, Liang J and Ueda T 2013 *Int. J. Adv. Manuf. Technol.* **68** 465–471

[135] Wang H, Zhou W, Cui Y, Wang G and Shum P P 2013 *J. Nanosci. Nanotechnol.* **13** 4581–4586

[136] Abdi O, Wong K C, Hassan T, Peters K J and Kowalsky M J 2009 *Opt. Commun.* **282** 856–861

[137] Atakaramians S, Afshar S V, Ebendorff-Heidepriem H, Nagel M, Fischer B M, Abbott D and Monro T M 2009 *Opt. Express* **17** 14053–14062

[138] Kou J L, Qiu S J, Xu F, Lu Y Q, Yuan Y and Zhao G 2011 *IEEE Photonics Technol. Lett.* **23** 1712–1714

[139] Kou J L, Qiu S J, Xu F and Lu Y Q 2011 *Opt. Express* **19** 18452–18457

[140] Liu Y, Meng C, Zhang A P, Xiao Y, Yu H and Tong L 2011 *Opt. Lett.* **36** 3115–3117

[141] Feng J, Ding M, Kou J L, Xu F and Lu Y Q 2011 *IEEE Photonics J.* **3** 810–814

[142] André R M, Becker M, Dellith J, Rothhardt M, Zibaii M I, Latifi H, Marques M B, Bartelt H and Frazão O 2015 Bragg grating fabrication on tapered fiber tips based on focused ion beam milling *24th Int. Conf. Optical Fibre Sens.* vol 9634 (SPIE) pp 432–435

[143] Hodzic V, Orloff J and Davis C C 2004 *J. Lightwave Technol.* **22** 1610

[144] Ding M, Wang P, Lee T and Brambilla G 2011 *Appl. Phys. Lett.* **99** 051105

[145] Ding M, Zervas M N and Brambilla G 2011 *Opt. Express* **19** 15621–15626

[146] Bag S K, Wan M, Sinha R K and Varshney S K 2020 *Sens. Actuators, A* **303** 111836

[147] Nayak K P, Kien F L, Kawai Y, Hakuta K, Nakajima K, Miyazaki H T and Sugimoto Y 2011 *Opt. Express* **19** 14040–14050

[148] Schell A W, Takashima H, Kamioka S, Oe Y, Fujiwara M, Benson O and Takeuchi S 2015 *Sci. Rep.* **5** 1–5

[149] Takashima H, Fukuda A, Maruya H, Tashima T, Schell A W and Takeuchi S 2019 *Opt. Express* **27** 6792–6800

[150] Yan H T, Liu Q, Ming Y, Luo W, Chen Y and Lu Y Q 2013 *IEEE Photonics J.* **5** 4800706–4800706

[151] Wieduwilt T, Dellith J, Talkenberg F, Bartelt H and Schmidt M A 2014 *Opt. Express* **22** 25333–25346

[152] Warren-Smith S C, André R M, Dellith J, Eschrich T, Becker M and Bartelt H 2017 *Sens. Actuators, B* **244** 1016–1021

[153] Kou J L, Feng J, Ye L, Xu F and Lu Y Q 2010 *Opt. Express* **18** 14245–14250

[154] Kou J L, Feng J, Wang Q J, Xu F and Lu Y Q 2010 *Opt. Lett.* **35** 2308–2310

[155] Yuan W, Wang F, Savenko A, Petersen D H and Bang O 2011 *Rev. Sci. Instrum.* **82** 076103

[156] Nguyen L V, Vasiliev M and Alameh K 2011 *IEEE Photonics Technol. Lett.* **23** 450–452

[157] Li X, Shao Y, Yu Y, Zhang Y and Wei S 2016 *Sensors* **16** 1–12

[158] André R M, Warren-Smith S C, Becker M, Dellith J, Rothhardt M, Zibaii M I, Latifi H, Marques M B, Bartelt H and Frazão O 2016 *Opt. Express* **24** 14053–14065

[159] Sun J, Li J, Maier R R J, Hand D P, MacPherson W N, Miller M K, Ritchie J M and Luo X 2013 *J. Micromech. Microeng.* **23** 105005

[160] Ding M, Murugan G S, Brambilla G and Zervas M N 2012 *Appl. Phys. Lett.* **100** 081108

[161] Cordeiro C M B, De Matos C J S, Dos Santos E M, Bozolan A, Ong J S K, Facincani T, Chesini G, Vaz A R and Cruz C H B 2007 *Meas. Sci. Technol.* **18** 3075–3081

[162] Martelli C, Olivero P, Canning J, Groothoff N, Gibson B and Huntington S 2007 *Opt. Lett.* **32** 1575–1577

[163] Wang F, Yuan W, Hansen O and Bang O 2011 *Opt. Express* **19** 17585–17590

[164] Huang J, Alqahtani A, Viegas J and Dahlem M S 2012 Fabrication of optical fiber gratings through focused ion beam techniques for sensing applications *Photonics Global Conference (PGC)* pp 1–4

[165] Gomes A D, Ferreira M F S, Moura J P, André R M, Kobelke J, Bierlich J, Wondraczek K, Schuster K and Frazão O 2016 *Microwave Opt. Technol. Lett.* **58** 679–683

[166] Warren-Smith S C, André R M, Perrella C, Dellith J and Bartelt H 2016 *Opt. Express* **24** 378–387

[167] Zheng Y, Chen L H, Yang J, Raghunandhan R, Dong X, So P L and Chan C C 2017 *IEEE J. Sel. Top. Quantum Electron.* **23** 322–326

[168] Flores R, Janeiro R and Viegas J 2019 *Sci. Rep.* **9** 1–9

[169] Adamu A I, Wang Y, Correa R A, Bang O and Markos C 2021 *Opt. Mater. Express* **11** 338–344

[170] Xiao M, Nieto J, Machorro R, Siqueiros J and Escamilla H 1997 *J. Vac. Sci. Technol. B: Microelectron. Nanometer Struct. Process. Meas. Phenom.* **15** 1516–1520

[171] Valaskovic G A, Holton M and Morrison G H 1995 *Appl. Opt.* **34** 1215–1228

[172] Puygranier B A F and Dawson P 2000 *Ultramicroscopy* **85** 235–248

[173] Kbashi H J 2012 *J. Mater. Sci. Technol.* **28** 308–312

[174] Ebbesen T W, Lezec H J, Ghaemi H F, Thio T and Wolff P A 1998 *Nature* **391** 667–669

[175] Benabbas A, Halté V and Bigot J Y 2005 *Opt. Express* **13** 8730–8745

[176] Degiron A and Ebbesen T W 2005 *J. Opt. A: Pure Appl. Opt.* **7** S90–S96

[177] Polimeno P, Magazzù A, Iatì M A, Patti F, Saija R, Boschi C D E, Donato M G, Gucciardi P G, Jones P H, Volpe G and Maragò O M 2018 *J. Quant. Spectrosc. Radiat. Transfer* **218** 131–150

[178] Ashkin A 1970 *Phys. Rev. Lett.* **24**(4) 156–159

[179] URL `https://www.ozoptics.com/ALLNEW_PDF/DTS0080.pdf`

[180] Binnig G, Quate C F and Gerber C 1986 *Phys. Rev. Lett.* **56**(9) 930–933

[181] Lehenkari P P, Charras G T, Nykänen A and Horton M A 2000 *Ultramicroscopy* **82** 289–295

[182] Ramachandran S, Mikkelsen B, Cowsar L C, Yan M F, Raybon G, Boivin L, Fishteyn M, Reed W A, Wisk P, Brownlow D, Huff R G and Gruner-Nielsen L 2001 *IEEE Photonics Technol. Lett.* **13** 632–634

[183] Ramachandran S, Ghalmi S, Chandrasekhar S, Ryazansky I, Yan M F, Dimarcello F V, Reed W A and Wisk P 2003 *IEEE Photonics Technol. Lett.* **15** 727–729

[184] Sumetsky M and Eggleton B J 2005 *J. Opt. Fiber Commun. Rep.* **2** 256–278

[185] Qi L, Zhao C L, Yuan J, Ye M, Wang J, Zhang Z and Jin S 2014 *Sens. Actuators, B* **193** 185–189

[186] Li Q S, Zhang X L, Shi J G, Xiang D, Zheng L, Yang Y, Yang J H, Feng D and Dong W F 2016 *Sensors* **16** 1–9

[187] Hsiao T C, Hsieh T S, Chen Y C, Huang S C and Chiang C C 2016 *Optik* **127** 10740–10745

[188] Jin X, Sun C, Duan S, Liu W, Li G, Zhang S, Chen X, Zhao L, Lu C, Yang X, Geng T, Sun W and Yuan L 2019 *IEEE Photonics J.* **11** 1–8

[189] Peng J, Jia S, Jin Y, Xu S and Xu Z 2019 *Sens. Actuators, A* **285** 437–447

[190] Zhong X, Wang Y, Qu J, Liao C, Liu S, Tang J, Wang Q, Zhao J, Yang K and Li Z 2014 *Opt. Lett.* **39** 5463–5466

[191] Hill K O, Fujii Y, Johnson D C and Kawasaki B S 1978 *Appl. Phys. Lett.* **32** 647–649

[192] Xuan H, Jin W and Zhang M 2009 *Opt. Express* **17** 21882–21890

[193] Hill K O, Malo B, Bilodeau F, Johnson D C and Albert J 1993 *Appl. Phys. Lett.* **62** 1035–1037

[194] Mihailov S J, Smelser C W, Lu P, Walker R B, Grobnic D, Ding H, Henderson G and Unruh J 2003 *Opt. Lett.* **28** 995–997

[195] Slattery S A, Nikogosyan D N and Brambilla G 2005 *J. Opt. Soc. Am. B* **22** 354–361

[196] Zhang W, Huang L, Gao F, Bo F, Zhang G and Xu J 2013 *Opt. Commun.* **292** 46–48

[197] Şimşek E U, Şimşek B and Ortaç B 2017 *Appl. Phys. B* **123** 1–9

[198] Jiang Z, Dong J, Hu S, Zhang Y, Chen Y, Luo Y, Zhu W, Qiu W, Lu H, Guan H, Zhong Y, Yu J, Zhang J and Chen Z 2018 *Opt. Lett.* **43** 4743–4746

[199] Li Y, Pu S, Zhao Y, Zhang R, Jia Z, Yao J, Hao Z, Han Z, Li D and Li X 2019 *Opt. Express* **27** 35182–35188

[200] Keren S and Horowitz M 2003 *Opt. Lett.* **28** 2037–2039

[201] Villar I D, Zubiate P, Zamarreno C R, Arregui F J and Matias I R 2017 *Opt. Express* **25** 10743–10756

[202] Zhou X, Yu Q and Peng W 2019 *Opt. Lasers Eng.* **121** 289–299

[203] Zhang Y, Yuan L, Lan X, Kaur A, Huang J and Xiao H 2013 *Opt. Lett.* **38** 4609–4612

[204] Duan D W, Rao Y J, Hou Y S and Zhu T 2012 *Appl. Opt.* **51** 1033–1036

[205] Zhou A, Qin B, Zhu Z, Zhang Y, Liu Z, Yang J and Yuan L 2014 *Opt. Lett.* **39** 5267–5270

[206] Ding W, Jiang Y, Gao R and Liu Y 2015 *Rev. Sci. Instrum.* **86** 055001

[207] Qian Y, Zhao Y, Wu Q L and Yang Y 2018 *Sens. Actuators, B* **260** 86–105

[208] Chen J H, Zhao J R, Huang X G and Huang Z J 2010 *Appl. Opt.* **49** 5592–5596

[209] Deng M, Tang C P, Zhu T, Rao Y J, Xu L C and Han M 2010 *Appl. Opt.* **49** 1593–1598